HydroFlex

Flexibility of Generator and Converter

Recommendations for design of end-winding electric field grading

This project has received funding from the European Union's Horizon 2020 research and innovation programme under grant agreement No 764011.

HydroFlex

Increasing the value of hydropower through increased flexibility

Deliverable 4.8 Recommendations for design of end-winding electric field grading

Work package	WP4 Flexibility of Generator and Converter
Task	Task 4.4 Enhanced generator winding insulation system and performance testing
Lead beneficiary	SINTEF Energy Research
Authors	Torstein Grav Aakre, Jorunn Hølto, Athanasios Mermigkas, Henrik Enoksen, Espen Eberg
Due date of deliverable	28.02.2022
Actual Submission date	28.02.2022
Type of deliverable	Report
Dissemination level	Public

This project has received funding from the European Union's Horizon 2020 research and innovation programme under grant agreement No 764011.

Executive Summary

The field grading of hydrogenator stator bars is designed for operation at 50 Hz. Pulse width modulated voltage source converters (PWM-VSC) are more and more used for generator control in e.g., pumped hydropower. The PWM-VSCs produce a voltage with a content of higher frequencies. The design is therefore altered, and premature failure can occur due to a higher electric field or heat generation. This deliverable contains a literature review presenting different field grading solutions, including both commercial and new materials. Three available commercial tapes are chosen for experimental description of the frequency and electric field dependent properties. The experimental results are used as input for a numerical study of the resulting surface temperature and electric field.

The results show that the electrical conductivity of the field grading material is both frequency and field dependent, whereas almost independent of temperature. The results in this work support the fact that designers must choose between either field control or temperature controlby selecting a high or low conductive field grading material respectively. The dilemma is not as relevant at 50 Hz; however, it becomes important at frequencies above 1 kHz as the electricfield distribution and surface temperature are significantly altered. This is relevant when using PWM-VSC with a voltage shape consisting of a high switching frequency and fast rise time.

Table of Contents

Abbreviations

AC	Alternating current
DC	Direct current
ECP	External corona protection
FEM	Finite element method
FGM	Field grading material
FGT	Field grading tape
GLP	Grading to lower permittivity
GO	Graphene oxide
HV	High voltage
IFD	Inverter fed drives
MO	Metal oxides
OCP	Outer corona protection
PD	Partial discharges
PWM	Pulse width modulation
SC	Semiconductor
SiC	Silicon carbide
VSC	Voltage surge converter
ZnO	Zinc oxide

Terms and Definitions

Insulation	Main wall insulation tape for resin rich technology
Medium FGT	Tape with medium stress grading characteristics
Strong FGT	Tape with strong stress grading characteristics
Weak FGT	Tape with weak stress grading characteristics

1 Introduction

Connecting a pulse-width modulated (PWM) volage source converters (VSCs) to a hydropower generator implies new and different voltage load stress to the insulation and field grading systems. One main concern is the implications on the field grading at the end-winding as the voltage waveform from a PWM VSC consists of high frequencies. A typical example of such waveform is shown in Figure 1-1 for the phase-to-phase voltage in a), phase-to-ground voltage in b), and overshoots at the motor terminal in c). As can be seen from the figures, both the switching frequency and the rise time contributes to much higher frequencies in the high voltage generator/motor.

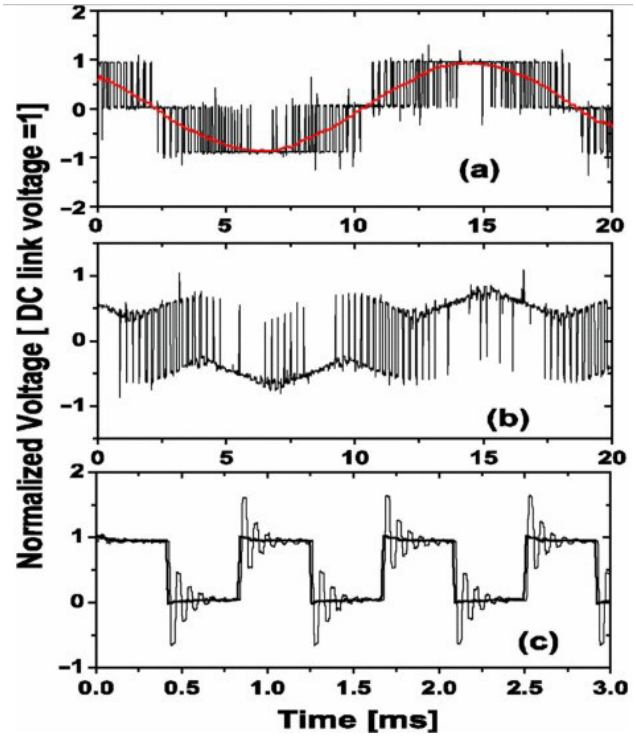

Figure 1-1: Typical waveforms from a PWM inverter drive: (a) Phase-to-phase voltage, (b) phase-to-ground voltage. (c) Overshoots at the motor terminal. The fundamental 60-Hz phase-to-phase voltage is also shown in (a) (Espino-Cortes, Cherney EA, and Jayaram 2007).

The main goal of Task 4.4 is, therefore:

To give recommendations for design of end-winding electric field grading by describing the impact of high frequencies on surface temperature and electric field of the field grading system with basis in the current solution for 50 Hz.

Task 4.4 therefore includes a thorough literature study of possible new materials used on end-windings. The core of the work is experimental characterization of three field grading materials as a function of applied voltage, frequency, and temperature. Laboratory models of the end-winding will be developed to facilitate electromagnetic modelling of the surface electric field and temperature based on input from the experimental work. The modelling is finally verified by surface temperature measurements.

2 Literature survey

This literature review starts by defining basic concepts of field grading, such as the capacitive and resistive field grading methods. Then, the use of resistive field grading method is discussed on rotating machines with respect to traditional 50 Hz/60 Hz voltage application and voltage application governed by converters giving rise to higher frequencies. After that, the state-of-the- art of resistive field grading materials is defined and possible new field grading materials are described. This includes defining a base matrix and different filler materials. The literature review is concluded by a summary and outlook to why the test matrix is chosen in the experimental part of this project.

2.1 Basic concepts behind electric field grading

The electric field inside insulation in high voltage components are determined by the material properties and geometry. Those components need terminations in the ends. Such terminations are practically a sharp edge if nothing extra is done and works well for low voltage apparatus. However, for higher voltage levels, the enhanced electric field causes problems by facilitating both partial discharges and temperature rise. Special terminations should therefore be made by applying some sort of electric field grading. Electric field grading is an umbrella term that includes all measures for effective electric field control used in different applications.

Field grading was first achieved by a capacitive solution by controlling the geometry of the insulation system. Then resistive field grading materials (FGM) were proposed in the 1960s (Penneck and Taylor 1976; Virsberg and Kelen 1963; Zlupko 1976), enhancing or even replacing purely geometric field grading as in the case of cable terminations (Lupo, Tucci, and Vitelli 1995). The possible strategies for field grading are today:

1. Capacitive field grading where the capacitance is controlled by material properties and by the geometry. The geometry can be manipulated by conductive layers within the field grading volume or by the complete design.
2. Resistive field grading where the conductivity is responsible for grading the field.

The equipotential surfaces of a geometric controlled capacitive field grading can be achieved by carefully selecting electrode shapes or inserting floating potentials for field control. Typical examples are given Figure 2-1 for cables, and inside the mainwall insulation of a generator bar in Figure 2-2. An iterative approach in the design process must be employed to ensure the topological characteristics provide capacitances and corresponding impedances which create voltage divider ratios between all stages that ensure electric field is always kept below critical levels at all locations in the system. As permittivity is the major factor in this type of design, this makes the applied electric field distribution achieved independently of frequency and thus applicable to impulsive energisation cases. Capacitive field grading presupposes a relative permittivity high enough to distribute the electric field (under AC and impulsive conditions) (Mårtensson 2003).

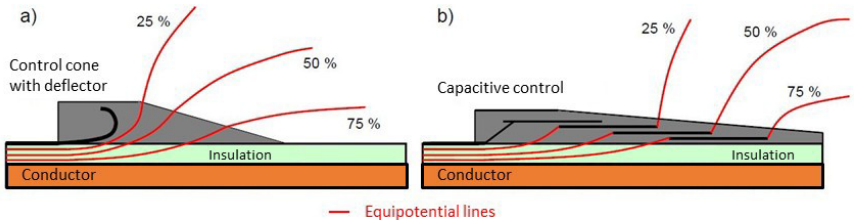

Figure 2-1: Principles of capacitive field grading of a cable (Senn 2010).

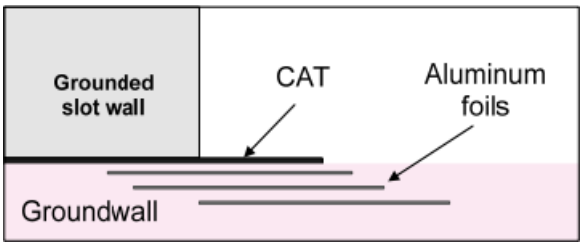

Figure 2-2: Geometry of a pure capacitive field grading solution where aluminium foils are embedded in the insulation for field control (E. Sharifi, Jayaram, and Cherney 2008). HV is at the bottom of the figure.

The resistive field grading method is a spatially distributed voltage divider along a stressed surface, as shown in Figure 2-3, where the permittivity and conductivity of the materials are specially selected. This method is used when compact designs are of prime interest to the system. The field grading is less functional at higher frequencies due to the high resistive impedance ($Z_R = R$) with respect to low capacitive impedance ($Z_C = 1/\omega C$). Surface discharges occur in the gaseous phase, thus by utilising resistive field control (in a form of a semiconductive layer) power available for discharges can be limited. In Figure 2-3, the equivalent circuit is valid only if the thickness of the insulation is much greater than that of the semi-conductive material above it. If the field grading layer is thick, permittivity and conductivity normal to the layers should be also examined.

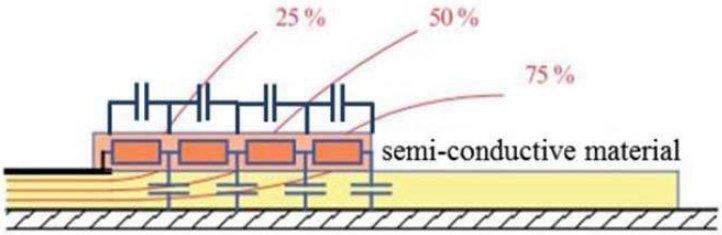

Figure 2-3: Sketch of resistive field grading (Cigré and Comité d'études D1 2019). The high voltage is applied on the bottom, whereas ground is the thick black line in the upper left corner. The insulation is coloured yellow.

The level of electric field grading depends on the difference between the conductivity and permittivity of the FGM to that of the insulation. If the difference is low, then the electric field at the interface between the materials is high. Thus, high permittivity materials are needed to keep the field grading layer thin.

Materials with a constant conductivity (linear FGM) cannot grade the electric field properly, as opposed to materials with electric field dependent conductivity (non-linear FGM) (Mårtensson 2003) (Espino-Cortes, Jayaram, and Cherney 2006). Utilizing a linear FGM results in an elevated electric field at the screen edge, though lower compared to if it was not installed in the first place. For an efficient reduction of field, resistivity should be low enough to achieve more even field distribution, however if the FGM is applied at a short length, the electric field might just concentrate at the other end of the FGM. This is not the case for a non-linear FGM, as the electric field peak of the linear case is non-existent and thus the formation of a considerably high electric field region at its end is much less probable (Mårtensson 2003), as seen in Figure 2-4.

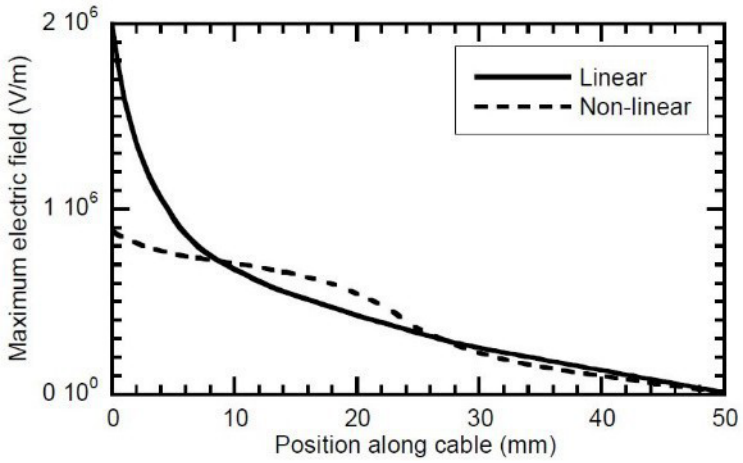

Figure 2-4: Comparison of linear and non-linear field grading material use in terms of the maximumelectric field across the cable length [6].

The conductivity is a function of temperature and therefore thermal balance needs to be taken into consideration. Transient energisation that involves short time scales must have a significantly reduced resistance to obtain proper electric field grading, thus leading to high losses (Mårtensson 2003). Non-linear FGM can increase their conductivity vastly when surpassing a specific field level, thus the losses at power frequency can be kept low, while providing effective field grading during transients. This makes them ideal in mitigating localised high electric fields (appearing at protrusions) in addition to high field stresses due to fast rising impulses, while achieving more compact designs at the same time. However, the heat produced in the critical region must be low enough to avoid thermal destruction of the FGM, meaning that Joule heating should be taken into consideration when designing such systems.

Both geometry optimalization and material choices are important strategies for optimal field grading. That is, a vast number of possibilities are available, where one optimal field grading solution for one case is not necessary the best solution in another case. For example, the field grading of large cables often utilizes a geometric shield for capacitive field control, whereas generator bars with much smaller available space use a resistive field grading at the end-windings. The scope of this report is to investigate the field grading in the end-winding of the generator bars; thus, the resistive field grading has a special focus in this report. The most important field grading possibilities are compiled in Figure 2-5.

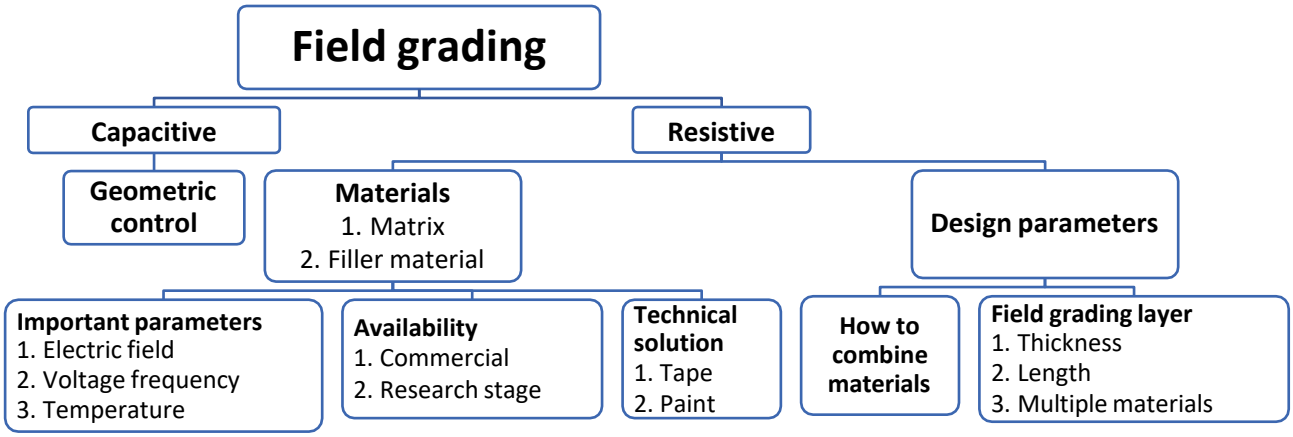

Figure 2-5: Field grading materials composition, application, forms available and what affects their properties. Notice the high number of combinations of how a material can be applied, producing quite different effects.

2.2 Applications on stator bars of electrical machines

The stator of a generator consists of an iron core with slots. Generator bars with copper conductor and insulation are placed inside the slots. The generator bars are covered with a semiconductive coating as outer corona protection (OCP) in the part that is inside the slot to avoid PDs occurring between ground insulation of the bars and the stator core. The OCP layer extends outside the slot, and to prevent PDs at the end of the OCP, field grading must be applied for all machines above 6 kV. This is also called end corona protection — (ECP), which gives a smoother potential distribution along its surface. Generator bars have a rectangular cross section with little available space; thus, a geometric field grading is inconvenient, and a compact resistive field grading system is preferrable. Researchers have adopted a surface field of 0.6 kV/mm as a design level for stress grading materials (Wheeler 2005). The common choice for ECP is to use SiC fillers in either the form of a tape or a paint (J. R. Weidner, Staubach, and Schmidt 2011). However, because of quality differences of SiC based FGM, even between batches from the same manufacturer, as well as high power loses causing thermal issues, research on other nonlinear filler materials has expanded (Donzel et al. 2016). Important design parameters for the ECP in the end-winding are:

- Paint or tape based
- The amount of overlap of ECP with the OCP
- The thickness, and number/length of the layers in the case of tapes
- Use of tapes with different field grading properties to optimise the electrical field grading design
- Double shielded configuration (Kimura and Hirabayashi 1985), (Staubach 2012)

The design of an end-winding is a trade-off between electric field control and thermal control. A highly conductive field grading tape (FGT) reduces the maximum electric field in the end-winding region but at the same time increases heat production and temperature A factor that complicates matters further is that the electrical conductivity can be altered by the vacuum pressure impregnation process and the fact that normal operational temperature is well above room temperature (Naeini, Cherney, and Jayaram 2019).

2.2.1 Typical stresses under power frequency

Under normal operational conditions, the temperature rise due to Joule heating is negligible. However, ECP could heat up and thus have its resistance lowered, due to the thermal losses of the copper winding conductor underneath it. The ECP should therefore be designed in a way that no thermal runaway effect occurs, which occurs when the ECP heats up and becomes more conductive leading to a positive feedback loop (instability). The maximum test voltage can for hydrogenerators be $4 \cdot U_N$, which is about the line-to-ground voltage under normal operation conditions sevenfold, might lie the limit ECP can withstand, even when applied for such short duration, in order to continue to operate properly (Cigré and Comité d'études D1 2019).

2.2.2 Typical stresses with pulse width modulated voltage source converters

External control of generators implies for example for variable speed drive applications the use of PWM-VSC. The PWM-VSC has the benefit of controlling the magnitude, phase angle and frequency of the output voltage. Operation using PWM-VSC at higher voltages is preferable compared to using high current due to the power limitations of components in electrical machines and cables (typically 1500 A) (Shakweh 2001) (Espino-Cortes, Cherney EA, and Jayaram 2007). However, PWM-VSC introduces high switching frequencies that is far above the design for the field grading system (tens of kHz).

FGM that perform satisfactorily under power frequencies, could still experience premature ageing and ultimate failure when exposed to PWM-VSC, even though multi-level converters nowadays utilise much shorter voltage steps. This is caused by narrow rise time impulses, in the order of some hundred nanoseconds, being generated at the converter output propagating towards the connection leads. This constitutes the main deterioration problem for stators rated higher than 6 kV (Stone et al. 2011; Stone and Sedding 1993). The FGM react differently when voltages with a wide band of frequencies are applied. Furthermore, frequency dependent capacitive current propagating through the main insulation will detrimentally affect the field grading. Higher frequencies will result in a steeper voltage rise and thus higher electric fields and PDs might occur on the FGM.

The higher current leads to thermal hot spots or even PDs may appear on the FGM when under PWM-VSC operation. One example of such thermal hot spots is seen in Figure 2-6. Thermal hotspots are seen both where the OCP ends (middle of the figure) and the FGM continuous, but hotspots are also seen next to the iron core (left).

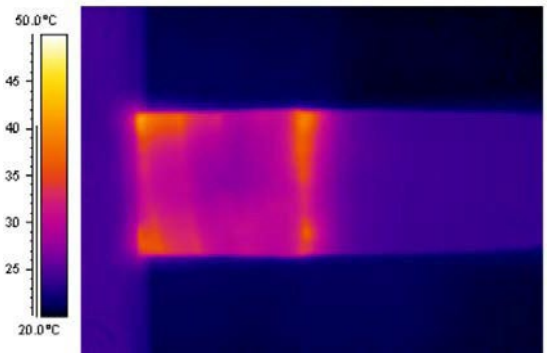

Figure 2-6: Temperature profile along the end-winding of a 13.8 kV motor bar energized with 5 kHz repetitive impulses (Emad Sharifi, Jayaram, and Cherney 2010b).

2.2.3 Design strategies for fast rise times

It is possible to either modify the applied voltage or the field grading material for a better field grading of the generator bar end-winding. A step towards the former is by introducing dV/dt filters, using multi-level VSC and reducing the length of cables between converter and generator terminals. However, two and tree level VSC are more reliable and less expensive than multilevel converters, which exaggerates the problem. In addition, PWM-VSC, cause problems on FGM both in terms of elevated electric fields and in hotspot creation (Espino-Cortes, Jayaram, and Cherney 2006).

For high frequency voltages, the OCP material can be too weakly conductive. This creates a high electric field at the stator slot exit during power electronic converter stress. This is in contrast to during normal operating conditions (50 Hz) where the highest electric field shifts towards the FGM as intended (Espino-Cortes, Cherney EA, and Jayaram 2007). This can be solved by adding a high-conductivity coating after the slot exit, as trying to increase the conductivity of the whole semiconductor will increase eddy current losses in stator laminations, or even short-circuit the laminations. The high-conductivity paint can be applied after installation of the stator bars. A proposed conductivity value of a semiconductive paint is two orders of magnitude higher than OCP semiconducting coating (Espino-Cortes, Cherney EA, and Jayaram 2007).

Thus, both OCP and ECP should be designed together to make sure field lines are evenly distributed even at high dV/dt conditions (Espino-Cortes, Cherney, and Jayaram 2005). Another possibility to reduce the electric field is to apply multiple layers of ECP materials with different properties as in (Hu et al. 2018), where, three ECP layers exhibited the most uniform field distribution and also showed the lowest losses (one order of magnitude less than the two-layer case) (Hu et al. 2018). The three layers correspond to, medium, medium-high and high resistivity.

In another example, (Espino-Cortes, Jayaram, and Cherney 2006), two field grading layers were proposed in order to reduce temperature rise of FGM when driven PWM-VSC, Figure 2-7. The layer overlapping the semiconductor, could have constant conductivity, however lower than the semiconductor's which was as low as 10^{-2} S/m. Selecting a conductivity value of 10^{-4} S/m for this layer, reduced the accumulated surface charge by four orders of magnitude, and thus the inception of hot-spots, while this 2-layer design also worked satisfactorily at power frequency (tests conducted for 20 kV rated cable ends at 60 Hz).

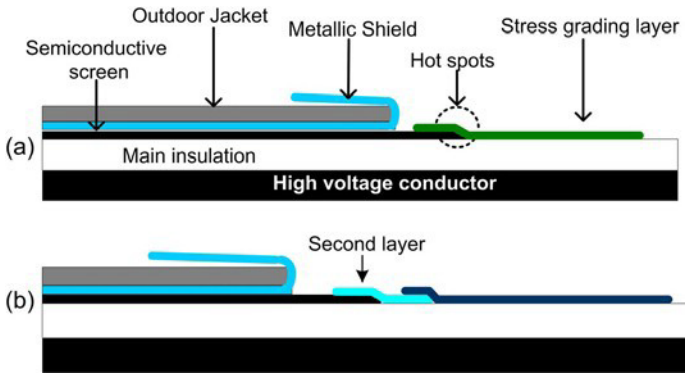

Figure 2-7: Design of two different layers of FGMs to avoid hot spots (Espino-Cortes, Jayaram, and Cherney 2006).

2.3 Resistive field grading materials

In general, a single material, e.g., epoxy, SiC, etc., does not meet all the design criteria needed for making a functional ECP. Two or more materials need to be combined where the different materials contribute with different important properties, in which the total design works well. A base material (host matrix) is usually selected for its mechanical properties or ease of fabrication, whereas the filler has the electrical properties needed. The base material can be a polymer like elastomer, hot melt compound or a thermosetting resin. Particle fillers are dispersed inside the matrix, and can be carbon black, or inorganic (ceramic) fillers. To produce a high-quality FGM is hard, especially when the intended non-linearity is high (Yang et al. 2018).

Non-linear materials show a temperature dependent behaviour, which is often described by their activation energy W_a of the Arrhenius equation. However, this behaviour is also a function of electric field strength and is most noticeable below the switching field strength. In general, for materials where the contact resistance is the important mechanism governing the conductivity, the conductivity is weakly temperature dependent, but is highly field dependent (Emad Sharifi, Jayaram, and Cherney 2010a). Between 20 °C and 120 °C the conductivity is affected mainly by a rise in contact resistance (Yang et al. 2018). With rising temperatures, the expanded matrix "disconnects" already existing conducting paths, thus raising the switching field strength. In turn the expanding matrix would lead to lower pressures between filler particles leading to lower contact resistance (Yang et al. 2018).

2.3.1 Mathematical description of conductivity of resistive field grading materials

It is beneficial to describe the observed behaviour mathematically. The typical field dependence of DC conductivity is shown in Figure 2-8 The base DC conductivity σ_0 is defined as a relatively flat range of conductivity at low electric field levels and shown as area ①. The AC conductivity of non-metallic materials are considerably higher compared to DC conductivity (Pradhan et al. 2016). The switching field strength E_1 is the field strength when the material becomes abruptly more conductive. The switching field strength can also be defined as the electric field level needed to reach a specific current density ②. The switching field can be adjusted by varying material characteristics of the composites. Theoretical studies have shown that the percolation threshold concentration [1] is only 15% volume for randomly dispersed spherical filler particles (Stauffer and Aharony 1994). In practice however, there are dependencies on grain size distribution, shape, and the distribution of grains in the matrix. Thus higher concentrations than 15 vol% are practically needed and in the case of two phase mixture, two such thresholds can occur (Sarraute et al. 1999). These thresholds arise from interfacial layers displaying increased surface conductivity (Roman, Bunde, and Dieterich 1986) or particles connecting in more than one way (Berlyand and Golden 1994; Mikrajuddin et al. 1999; Sheng and Kohn 1982), e.g. edge and face connections (Mårtensson 2003). It is interesting to note that in 2D simulation, circular particles show a lower E_1 compared to irregular ones (Yang et al. 2018). At a particular electric field called the saturation field, the conductivity reaches its saturation value, σ_{sat}, and does not increase any further. This area is shown as ③ and it happens when the electric field surpasses its saturation field strength level, E_{sat} or E_2.

[1] Percolation threshold concentration is reached when the filler particles start to form unbroken chains through the composite material. This causes the resistivity of the composite to fall dramatically, thus

changing its properties.

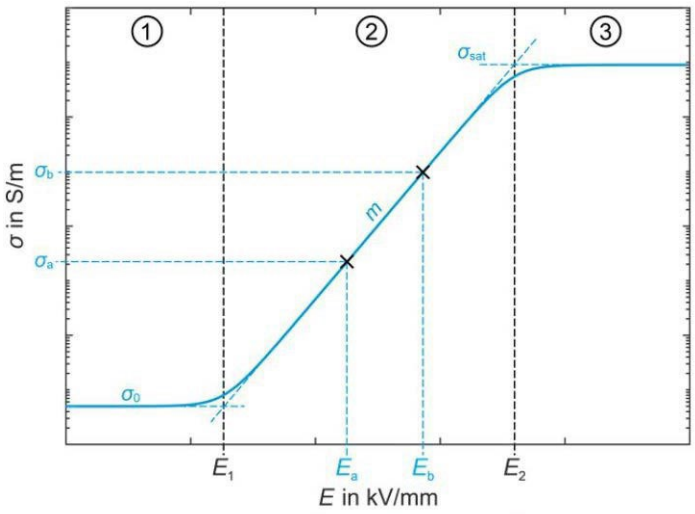

Figure 2-8: One example of a typical DC conductivity as a function of electric field for a non-linear fieldgrading material (M. Secklehner, Hussain, and Hinrichsen 2017).

Mathematically, the graph in Figure 2-8 can be described by (Maximilian Secklehner, Kosse, and Hinrichsen 2017):

$$\sigma_{DC}(E) = \sigma_0 \cdot \frac{\alpha_1 \left(1 + 10^{(n - n_0)\alpha_1 (E - E_1)}\right)}{\alpha_2 \left(1 + 10^{n \alpha_2 (E - E_2)}\right)} \cdot 10^{n_0 E} \tag{1}$$

where α_1 and α_2 are shaping variables usually equated initially to unity, n is the nonlinear coefficient, n_0 is the nonlinear coefficient of the base conductivity $\sigma_0 \cdot 10^{n_0 E}$ in ①. Thus, if $m_0 = 0$ then the base conductivity is field independent.

The slope m of the curve in the non-linear phase (marked ② in Figure 2-8) is called the nonlinear coefficient or the degree of nonlinearity. It is found directly from the figure as (M. Secklehner, Hussain, and Hinrichsen 2017):

$$m = \frac{\log \frac{\sigma_b}{\sigma_a}}{E_b - E_a}. \tag{2}$$

However, it is also possible to consider the current as a function of electric field instead of conductivity in Equation (1) as a function of electric field, normally following a power law:

$$I = I_0 (E / E_0)^{\alpha}, \tag{3}$$

where E is applied electric field, α is the nonlinear coefficient, I is the current, and I_0 and E_0 are constants dependent on the material. The above power law describes the current in the non-linear region as a function of voltage up to a range after which non-linearity coefficient becomes a function of voltage itself (Mårtensson 2003). The nonlinearity coefficient α is then:

$$\alpha(E) = \frac{\log I_b / I_a}{\log E_b / E_a} = 1 + \frac{\log \sigma_b / \sigma_a}{\log E_b / E_a}, \tag{4}$$

where γ_b, E_b, and γ_a, E_a are selected points in the linear part in a log-log plot of current vs electric field, like what was done in Figure 2-8 for the conductivity.

The most crucial parameters for designing FGM are the nonlinear coefficient α and the switching field E_1. These parameters are challenging to control. In practice, it is in most cases sufficient that α > 10. It is on the other hand harder to adjust E_1 to a particular application (Christen, Donzel, and Greuter 2010), as it would require to vary filler size distribution and their corresponding shape. An α between 10 and 20 is considered to mitigate locally created field enhancements. Whereas it is marginal benefits from a higher non-linearity (α > 20). Theoretical examinations show that α should be increasing with increasing inhomogeneity of the geometry (Christen, Donzel, and Greuter 2010). For resistive field control, nonlinearity stems either from particle-particle contact, or in the case of microvaristors, from internal grain boundaries (Greuter and Blatter 1990). In both cases double Schottky barriers are formed. Thus, each grain boundary increases the switching voltage by 3.2 to 3.4 V (Greuter and Blatter 1990) (Donzel, Greuter, and Christen 2011).

The nonlinear conductivity is not well understood. Measurements are therefore needed to describe the material in use. Experimental data are therefore curve fitted to different mathematical models, whichever fits the data best.

2.3.2 Matrix materials

The matrix material should provide mechanical support for the fillers and make it possible to include a variety of filler content. For matrix materials, the following families of materials are usually selected:

- *Thermoplastic polymers* (Xanthos 2005) like polyethylene (PE), polyvinyl chloride (PVC),polypropylene (PP), and poly(ethylene-vinyl acetate) (PEVA).
- *Thermoset polymers* (which in addition cross-link forming a network structure), like epoxy resin (Yang et al. 2018), alkyd resin (alcohol and organic acid) and polyurethane. These materials can also be the main ingredient of varnishes, coatings, and tapes. Cross-linked PE forms the thermoset XLPE, used as HV cable insulation in addition to warm shrink applications. Elastomers are wide-meshed thermoset polymers, usually applied in cable accessories.
- *Silicone rubbers* (VMQ) (Yang et al. 2018), (Cherney 2005; Donzel, Greuter, and Christen 2011; Meyer, Cherney, and Jayaram 2004; Momen and Farzaneh 2011). These can be further classified in high temperature vulcanizing silicone rubbers (HTV silicone), room temperature vulcanizing silicone rubbers (RTV silicone), and liquid silicone rubbers (LSR). VMQ can be delivered as tape, coating, or varnish.
- *Ethylene propylene rubber* (EPM, often incorrectly denoted as EPR) also used for extruded cable insulation and cable accessories, however it exhibits high dielectric losses and thus is used only up to voltage levels for distribution cables. Ethylene propylene diene rubber (EPDM rubber), finds applications as a cold shrink material (Yang et al. 2018) (Mårtensson 2003) (Pradhan et al. 2016).

2.3.3 Fillers

Fillers of different types are used to modify the permittivity and conductivity of the matrix material. The fillers can be distributed either homogeneously inside the matrix or have a gradient spatial distribution. The use of fillers is not limited to one type at once, as the use of multiple different fillers can improve the design.

The mechanism for determining the conductivity varies based on the filler type, and only when the filler concentration is above its percolation limit. Conductive fillers have an impact on the conductivity by their concentration as shown in Figure 2-9 for the most common conductive fillers carbon black and carbon nanotubes (CNT). CNT are commercially available but have not reached a broad range of applications yet. The diameter of CNTs is usually in the range of 1 nm to 50 nm.

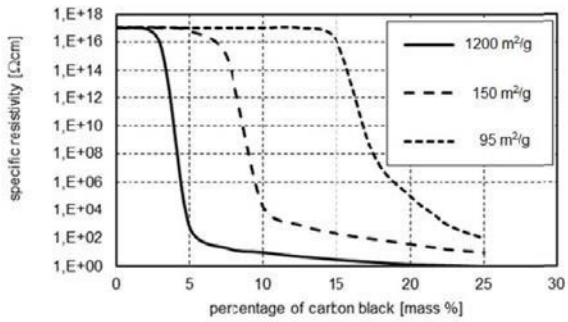

a) Effect of specific surface area of carbon black on the FGM resistivity (Cigré and Comité d'études D1 2019)

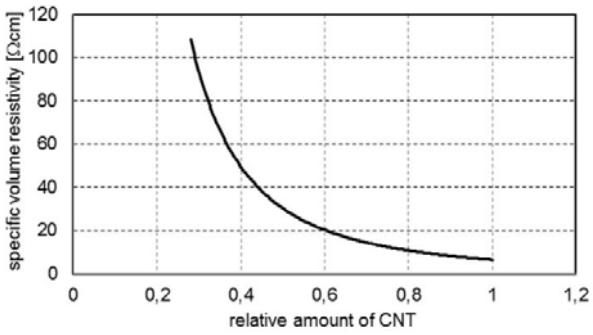

b) Specific volume resistivity as a function of the amount of carbon nanotubes (Cigré and Comité d'études D1 2019).

Figure 2-9: The effect of filler content of conductive particles to the specific resistivity.

The semiconductive fillers have an impact on the conductivity based on their properties. The most used non-linear semiconductive materials are based on SiC. For some applications ZnO is used, and other fillers are still under investigation and not ready for application yet. Typically, SiC are sharp edged bulky particles, used for grinding applications (no higher quality exist for power applications). Contact zones of SiC are through grains and are modelled by Schottky-like barriers. The geometry of such a SiC based composite is sketched in Figure 2-10.

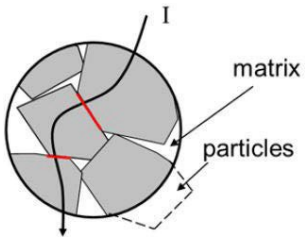

Figure 2-10: Illustration of an SiC based composite, with interparticle contact points marked in red, which are responsible for the macroscopic electrical properties of the composite (Donzel, Greuter, and Christen 2011).

The resistivity of the composite decreases with increasing particle size, as seen in Figure 2-11. The number of contact spots increase, thus reducing resistivity. However, SiC can be greatly affected by impurities, meaning that identical grain size SiC from different suppliers can have completely different properties. Thus, ECP in tape form can have huge specification differences in terms of tolerance of field control elements (Cigré and Comité d'études D1 2019). Comparison of two equally distanced conduction paths with fillers of different particle size, shows that the one with smaller particle size have more contact interfaces, thus higher E_1 and contact resistance. In terms of filler concentration, the higher it is, the lower the contact resistance and E_1 (Yang, He, and Hu 2015) (Yang et al. 2018). In addition, (Yang et al. 2018) concluded that if fillers are

distributed randomly, conduction path easier to be created by lower concentration and larger particle size, rather than the opposite (Nan, Shen, and Ma 2010). This effect is augmented for irregularly shaped fillers, thus the development of more and shorter conduction paths (Strümpler and Glatz-Reichenbach 1999; Yang, He, and Hu 2015).

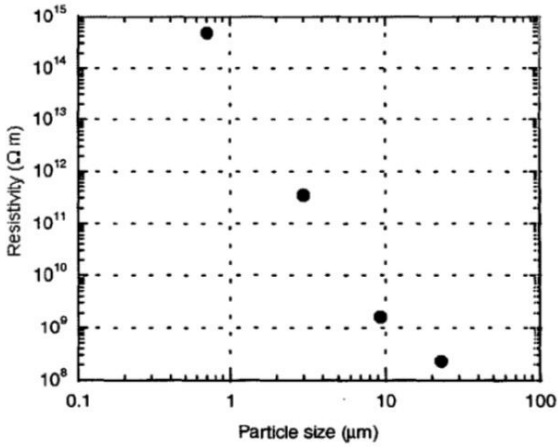

Figure 2-11: Resistivity as a function of particle size for SiC composites (Cigré and Comité d'études D1 2019) (Senn 2012).

Metal oxides, such as ZnO, SnO_2, and $SrTiO_3$, have a slightly different conduction mechanism than SiC. The nonlinearity of e.g., ZnO is caused by the microstructure of the ceramic particle itself, in contrast with Schottky-like barriers between SiC particles. In this case the grain boundaries inside the particles act as double Schottky barriers, which the current passes through as seen in Figure 2-12.. This means that ZnO microvaristors exhibit very high exponents of nonlinearity, that is, α from 20 to 50. In a ZnO/silicone rubber material, the switching field could be increased by having a smaller filler size, as well as irregular filler shape (Yang et al. 2018). In addition, existing conductive paths and contact resistance of the filler grains could also affect the switching field (Yang et al. 2018). Additional information on ZnO in terms of electrical, thermal and mechanical data analysis can be found in (Amerpohl et al. 2002; Glatz-Reichenbach et al. 1996; Gramespacher et al. 2003; Greuter et al. 2004; Haverkamp, Strobl, and Malin 2000; Rieux and Marugan 2002; Struempler et al. 1995).

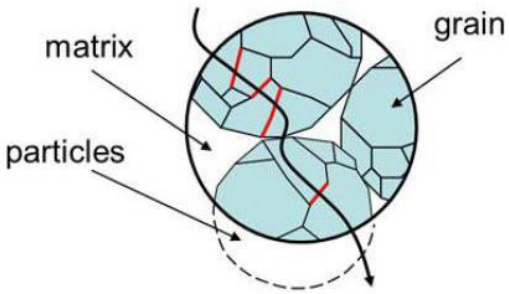

Figure 2-12: Illustration of an ZnO based composite, with inter-grain contacts points marked in red, which are responsible for the macroscopic electrical properties of the composite (Donzel, Greuter, and Christen 2011).

The conduction mechanism for SiC is tunnelling by field emission. Basically, close to the percolation threshold tunnelling through thin insulating layers separating the particles occur (Nakamura et al. 1997). For ZnO, like other microvaristor materials, non-linearity is inherent in the filler particles by domain walls inside the grains, and therefore easier to control. Tunnelling mechanisms caused by electric potential barriers existing at grain boundaries create non-linear conduction phenomena between particles (Greuter and Blatter 1990; Huey and Bonnell 2000; Stucki and Greuter 1990).

A typical plot of resistivity as a function of electric field for ZnO based composites and current as a function of voltage for SiC composites are shown in Figure 2-13 a) and b), respectively. It is found that ZnO has a higher nonlinearity than SiC, but both materials clearly show a nonlinear effect of electric field. Varistor technology (including ZnO) has sharper switching characteristic and higher non-linearity, which makes it more efficient at resistive field grading during impulsive voltages. In addition, with a relative permittivity between 10 to 15, refractive effects also contribute to the efficient field grading at high frequencies (Donzel, Greuter, and Christen 2011).

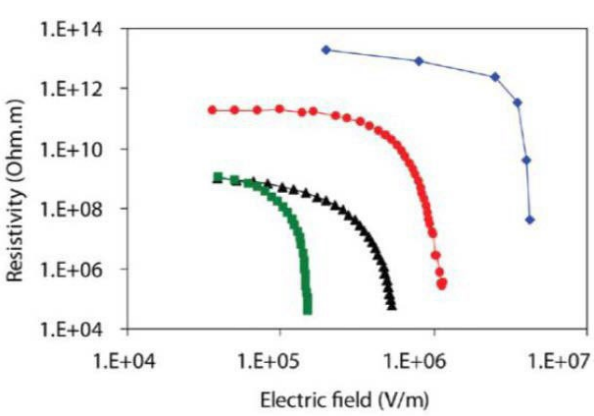

a) Resistivity as a function of electric field for different ZnO based composite materials (Donzel, Greuter, and Christen 2011).

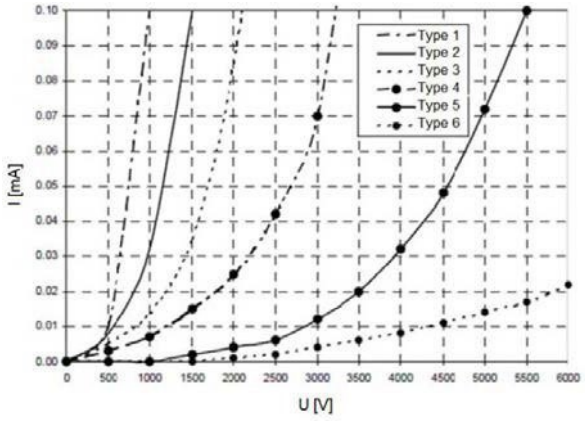

b) Current as a function of applied voltage for different SiC configurations, depending on SiC particles. The nonlinearity factor is α = 2 to 4 (Brandes, Hillmer, and Stebler 2008).

Figure 2-13: Resistivity and current as a function of electric field and voltage for ZnO and SiC, respectively.

Nowadays the most used FGM is composed of SiC fillers. Possible alternatives to SiC fillers can be based on ZnO, graphene oxide, SnO_2, as well as carbon black, or mixtures of various oxides, e.g., $BaTiO_3$, TiO_2, SiO_2, Fe_3O_4, CeO, and mica, (Mårtensson 2003; Emad Sharifi, Jayaram, and Cherney 2010a; Pradhan et al. 2016; Greuter and Blatter 1990; Wang et al. 2012; Mackevich and Hoffman 1991; Nelson and Hervig 1984; Onneby et al. 2001; Roberts 1995; Virsberg and Ware 1967; Wheeler et al. 2007a; 2007b). In terms of how they are applied, FGM in the form of tapes and paints (Brütsch and Hillmer 2006; Rivenc and Lebey 1999; Roberts 1995; J. Weidner 2008) are still being developed and improved. A detailed list of different candidate material fillers for modifying different properties are given in Table 2-1.

Table 2-1: Composite material properties that need to be achieved, and fillers that can achieve this according to literature (Pradhan et al. 2016).

Properties	Fillers
Electrical conductivity	Carbon black, carbon fibre, graphite, carbon nanotube, metal powders(Ni, Fe, Cu, Zn, Al)
Electrical stress grading	SiC, ZnO, $BaTiO_3$, graphene oxide
Tracking and erosion	SiO_2, $Al(OH)_3$ (ATH), or Al_2O_3, Melamine Cyanurate
Hydrophobicity	$CaCO_3$
Fire extinguishing	$CaCO_3$, $Al(OH)_3$ (ATH), MHSH, $Mg(OH)_2$, $Ca(OH)_2$
Thermal conductivity	SiO_2, ZnO, Carbon fiber, Graphite, Carbon nanotube, metal powders (Ni, Fe, Cu, Zn, Al), nitrides (AlN, BN)
Thermal stability	TiO_2, $BaTiO_3$
Mechanical strength	Carbon black, Graphite, Carbon nanotube, metal powders (Fe, Zn, Ag),MHSH
Dielectric constant	TiO_2, ZnO, $BaTiO_3$, Aluminium powder

A summary of different electrical parameters for combinations of fillers and matrices is shown in Table 2-2. The conductivity can be adjusted by the concentration of fillers (like SiC) in the matrix, but the non-linearity is reduced at high concentrations. The non-linearity is stable with low concentrations, but adding conductive nanoparticles weakens the non-linearity. On the other hand, for microvaristors (like ZnO) doping elements and sintering parameters can adjust the non-linearity quite easily. The switching field strength E_1 can be adjusted by changing the size of the grains, as larger grains correspond to lower number of boundaries between grains and thus lower E_1. Microvaristors can be added above the percolation limit, to ensure that small changes in doping does not affect the total resistivity, as the change can be quite severe for linear materials.

It has been shown that FGM conductivity variation as a function of electric field is much greater under DC than under AC application (Emad Sharifi, Jayaram, and Cherney 2010b). Directional dependent DC conductivity values give inaccurate results when used for repetitive impulsive voltages and high frequencies energisation in general. On the other hand, directional dependent conductivity values of the FGM and the semiconductor under AC voltage stress give accurate results under impulsive stresses and high frequencies. Especially the latter is important in analysing the electric field enhancement by impulsive voltages. In addition, DC conductivity of the FGM is not representative of its behaviour under very high electric field, rather such parameters can be identified through transient FEM analysis using AC conductivity and anisotropic modelling (Emad Sharifi, Jayaram, and Cherney 2010b).

Table 2-2: Properties of non-linear materials found in literature (Cigré and Comité d'études D1 2019). References in table as they are given in (Cigré and Comité d'études D1 2019). It is important to note that the notation $EEEE_{bbbb}$ in this table is the same as $EEEE_{1111}$ in Figure 2-6.

Filler	Matrix	% vol	α	E_b kV·mm^{-1}	σ_0 S/m	Ref.
Carbon black [CB]	polyolefins / EPDM		0.2...2.5		≈3×10^{-12}	[Egiziano 1995]
SiC/CB	EPDM	0.117	≈4	≈0.22	≈5×10^{-16}	[Mårtensson 1998][1]
SiC/Fe3O4	polybutadiene	0.432/0.08	≈3.1	≈0.027	≈2.7×10^{-10}	[Okamoto 2001][1]
		0.432/0.08	≈1.7	≈0.071	≈2.5×10^{-6}	
sealing mastic			6.4	0.18	≈9.2×10^{-14}	[Sonerud 2012]
SiC - 0.7 µm	EPDM	0.4	≈4	≈1.5	≈5.4×10^{-18}	[Önneby 2001][1]
SiC - 3.0 µm			≈5.8	0.6	≈3.3×10^{-17}	
SiC - 9.3 µm			≈3.1	<0.1		
SiC - 23 µm			≈3.4	<0.1		
GO	VMQ	0.03	15	3.3	≈3.8×10^{-16}	[Wang 2012a][1]
		0.05	17	1.8	≈1.7×10^{-16}	[Wang 2012b][1]
PANI-EB+graphite	silicone rubber	0.25	≈10	≈10		[Pelto 2004]
ZnO	silicone rubber	0.35	22	1.3...1.7	10^{-12}	[Donzel 2011]
ZnO + boundary formers [Bi2O2/Sb2O3] + conductivity enhancers [CoO/MnO]	LLDPE	0.25	32	0.92		[Lin 2008]
		0.33	31	0.59		
		0.4	22	0.43		
		0.45	18	0.26		
ZnO	epoxy	0.48	≈14	1.23	≈7×10^{-11}	[Secklehner 2017b]
ZnO	silicone rubber	0.39	10...11	0.50...0.82		[Yang 2015]
ZnO	epoxy	0.42	≈23	0.3	2x10^{-10}	[Matsuoka 2015]
Iriotec 7000®-Series (ATO)	Epoxy, blanket coating		2...5		10^{8}...10^{12} Ω surface resistance	[Greb 2015]
MFF1 (ATO)	epoxy, 38 wt%		≈3.6		6.5×10^{-14} @30 °C	[Secklehner 2013]
MFF2 (ATO)	epoxy, 38 wt%		≈3		3×10^{-14} @30 °C	[Secklehner 2015]

[1] Results from fitting plot in publication

2.3.4 New approaches for fillers under development

Commercial field grading materials are created by adding suitable conducting or semi-conducting particles to a matrix. New approaches include intrinsic conductive polymers, graphene oxide, tin dioxide SnO2, and functionally graded materials.

The intrinsic conductive polymers include polypyrrole, polythiophene, and polyaniline. Polyaniline (PANI) is of prime importance for the HV industry as it is nowadays one of the most environmentally stable and intrinsically conductive polymers. Applications have been reported for cables (semiconducting layers) and as fillers in polypropylene films used for capacitors. Its emeraldine base state (PANI-EB) is an intrinsic semiconductor with σ =10^{-9} S/m to 10^{-8} S/m (DC)

with α = 2.8. It is considered that PANI-EB is manufactured with higher non-linearity than SiC, however not expected to reach the ZnO levels (Cigré and Comité d'études D1 2019).

Graphene oxide is a non-linear FGM which can yield composites of α ≈ 16. Conductivity as a function of electric field for different graphene oxide loadings is shown in Figure 2-14 The percolation limit of graphene oxide in VMQ is found to be 2 to 3%.

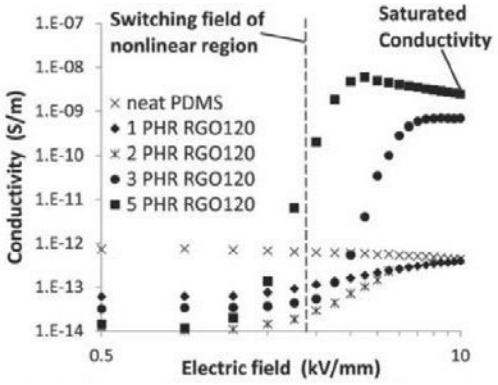

Figure 2-14: Conductivity as a function of electric field for different graphene oxide loadings (Wang et al. 2012).

Graphene nanocomposites combined with inorganic materials are being investigated, as they could help to create very high dielectric constant FGM as shown in Figure 2-15 a). However, in experiments with graphene oxide the dissipation factor increases orders of magnitude when the percolation threshold is reached, as seen in Figure 2-15 a).

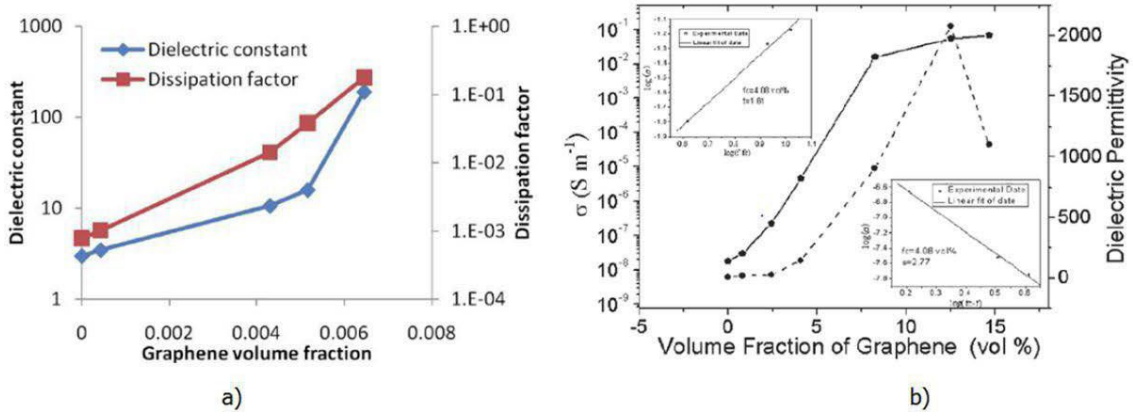

Figure 2-15: a) relative permittivity as a function of graphene oxide volume fraction (Cigré and Comité d'études D1 2019) (Pang et al. 2010) and b) conductivity as a function of graphene oxide volume fraction (Cui et al. 2011).

Tin dioxide (SnO_2) performs similar to ZnO, as it also exhibits conduction through the grain boundaries inside the microvaristor particles in a non-ohmic fashion. SnO_2 has a higher thermal conductivity, higher switching field and lower leakage current compared to ZnO. However, as in the case of ZnO, the sintering process affects the conductivity. To make matters worse for SnO_2, there are Joule heating issues due to its high porosity structure, meaning poor particle contact. In addition, pure SnO_2 needs sintering aids in order to be sintered into a ceramic, for example CuO in low concentrations (0.5 to 2 mol%) as more inevitably leads CuO forming conductive paths. As

an example, $SnO+Co_3O_4-Nb_2O_5-Cr_2O_3$ has exhibited nonlinearity of up to α = 75 (Cigré and Comité d'études D1 2019)

Both ZnO and SnO_2 have been investigated in literature, however ZnO have not proven to be able to substitute more traditional materials, like SiC, as of today. Extended knowledge of the system and its behaviour is needed in order to try new material concepts, due to the vast number of different parameters and corresponding degrees of freedom to be investigated. It is a very limited market share for such materials development, and even the expected improvement in performance seems small, thus driving further research of such materials in novel use to almost a halt.

A material with decreasing permittivity values (Grading to Lower Permittivity - GLP) can be obtained by using a mix of small particles of high permittivity and large particles of lower permittivity. To achieve a spatial distribution of particles a centrifugal force is applied before the matrix is cured. With this method a GLP-FGM can be produced with graded permittivity along the centrifugal direction as illustrated in Figure 2-16

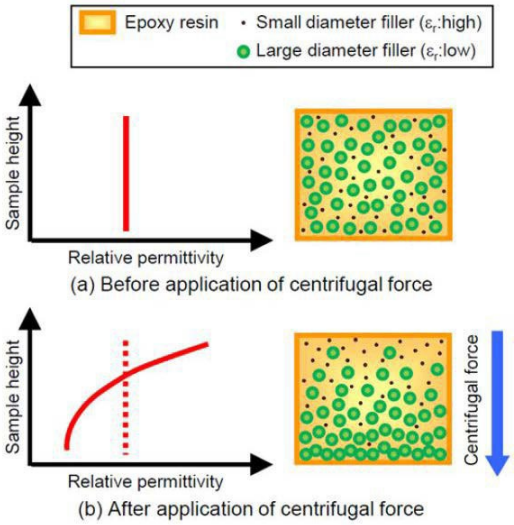

Figure 2-16: An example of how to utilize the centrifugal force to obtain a permittivity gradient in the material along the axis of rotation (Hayakawa et al. 2014).

To create permittivity functionally graded materials, different fillers are used that are out of the scope of this report. However, for completion purposes, Table 2-3 is provided to the interested reader. It is also worth noting that for the composite materials used for refractive field control (high permittivity), the percolation threshold need not be reached (Greuter and Blatter 1990). In theory, non-linear FGM could improve refractive field grading and avoid the unwanted thermal issues simultaneously, however such materials exhibiting strong non-linear permittivity as a function of electric field do not exist yet. Research in that direction is being active though (Zhang et al. 2020). The permittivity of such composites is often temperature dependent and sometimes also being affected by electric field strength. In terms of specific materials, $BaTiO_3$ and aluminium powder can be used to increase the dielectric permittivity of SiR (Cherney 2005). In addition, permittivity and losses of FGMs containing ZnO are higher, however thermal conductivity is enhanced (Pradhan et al. 2016).

Table 2-3: Properties of filler particles used in order to create permittivity functionally graded materials(Cigré and Comité d'études D1 2019).

	Epoxy resin	Hardener	Filler		
Chemical structure	BPA epoxy resin	Anhydride-type	Al_2O_3	TiO_2 rutile crystal	SiO_2 crystal
Shape	-	-	Spherical	Angular	Angular
Relative permittivity (1kHz, 30℃)	3.5 (at mixed condition)		9.3	114	4.5
Specific gravity [g/ml]	1.19 (at mixed condition)		3.95	4.2	2.65
Viscosity [Pa*sec] (30℃)	1.7 (at mixed condition)		-	-	-
Mean diameter [μm]	-		3.21	0.672	5.89

Anisotropic effects could appear in an FGM, if the filler material has a high aspect ratio and it happens to orient itself in a particular direction during the formation process. This could cause an unwanted increase in conductivity in a particular direction. However, this phenomenon has been exploited, in order to make compound varistors (Ishibe et al. 2013). This was achieved with the application of an electric field during curing, thus orienting the filler materials in percolation paths across the field lines. That way percolation is also achieved with usage of less filler material that that needed for achieving percolation and could potentially be used for FGM.

FGM utilising microvaristors can suffer from lack of mechanical strength, as a high concentration of (relatively large size) particles is needed, to reach the percolation limit and thus behave in a non-linear manner. In order to improve this, bridging conductive particles can be used, like carbon black (Jonsson and Palmqvist 2008) and carbon nanotubes. This concept improves mechanical strength by reducing the amount of the filler particles needed, as the filler particles can be connected with these bridging particles.

2.4 Summary and research scope based on current knowledge

In rotating electrical machines, a semiconductive coating (OCP) is applied to the outer surface of all stator bars before they are inserted in their slot, to avoid PDs occurring between the bars and the stator core. OCP extends outside the slot, and in order to prevent PDs at the OCP's end, field grading must be applied for all machines above 6 kV. This end corona protection should reduce the surface electric field below the surface discharge threshold level. A practical maximum design surface electrical field of 0.6 kV/mm is adopted among researchers and should be valid at voltages even as high as 4.5 times of what is expected during normal operation due to generator acceptance test criteria. To achieve satisfactory field grading important design features are length of the overlap between FGT and OCP, the length of the FGT, and the number of FGT layers to control the conductivity.

The field grading is designed to perform satisfactorily under power frequencies and is expected to perform differently when voltages with a wide band of frequencies are applied. As renewable energy sources are connected to the grid, extensive use of power converters is expected. These PWM-VSC generates extremely narrow rise time impulses with a high repetition rate, which might

reach the connector leads. To avoid premature failure caused by electric breakdown the field grading design might need to be altered when hydrogenerators are connected PWM-VSCs, even though multi-level converters nowadays generate much lower voltage steps. A high switching frequency with a steep voltage rise result in subsequently higher electric field levels and possible Joule heating. Thus, important failure mechanisms are thermal hots spots or even PDs at local points with high electric field. Furthermore, frequency dependent capacitive current through the main insulation will detrimentally affect the field grading.

Different strategies can be attempted to achieve good field grading under exposure of high frequencies. To employ resistive field grading for short time scales resistance must be significantly reduced, which typically leads to high losses and thermal hots spots. Capacitive field grading designed using field grading material with linear properties may be difficult, whereas a non-linear material can provide efficient field control under various conditions, (Mårtensson 2003) especially in the case driven by PWM-VSC (Espino-Cortes, Jayaram, and Cherney 2006). Non-linear material changes its electric properties and becomes more conductive when an electric field level is surpassed. Thus, losses can be minimised at continuous operation, without affecting the performance at higher electric fields and transients.

The most used non-linear FGM is composed of a base polymer matrix with selected SiC fillers. SiC fillers are, however, difficult to fit to a specific design as the grain properties are difficult to control in the manufacturing process. Therefore, extensive research on alternative FGMs is available, based on use of fillers as graphene oxide (Greuter and Blatter 1990; Mårtensson 2003; Wang et al. 2012), (Pradhan et al. 2016), or blends of different oxides, e.g., $BaTiO_3$, TiO_2, SiO_2, Fe_3O_4, or CeO (Mackevich and Hoffman 1991; Nelson and Hervig 1984; Onneby et al. 2001; Roberts 1995; Emad Sharifi, Jayaram, and Cherney 2010a; Virsberg and Ware 1967; Wheeler et al. 2007a; 2007b), (Donzel, Greuter, and Christen 2011). A promising alternative is based on use of ZnO (Donzel, Greuter, and Christen 2011) (Yang et al. 2018), which behaves as a microvarisor and exhibits a conductivity dependent on electric field, with greater and more stable non-linearity compared to traditional SiC FGMs (Yang et al. 2018). In addition, permittivity and losses of FGMs containing ZnO are higher, whereas the thermal conductivity is enhanced (Pradhan et al. 2016). However, it should be noted that no ready-made materials containing ZnO in either tape or paint form are available on the market, with the sole exception of cable terminations (Donzel, Greuter, and Christen 2011).

The current field grading technology is optimized for 50 Hz, whereas the field grading is degraded when high frequencies are applied. It is therefore necessary to investigate how the current solution responds to higher voltage frequencies. No new materials are commercially available in an FGM solution, including the promising ZnO. Using non-commercially available FGM solutions would require a long in-house material production time. This work focuses, therefore, on the frequency dependency of the current FGM solution based on SiC, and from that give recommendations to how to deal with the lost field grading at higher frequencies.

3 Methodology

The findings in the literature showed that higher electric fields and thermal hotspots are expected in the end-winding when connecting PWM-VSC to generators. The literature review focused on possible field grading materials due to the scarce description of frequency dependence of the existing field grading materials. This work therefore focused on how high frequency voltage stresses influence the surface electric field and surface temperature of existing material solutions. The surface electric field is not possible to measure at higher frequencies as electrostatic voltmeters are only functioning up to a few hundred Hz. The scope is therefore to characterize the involved materials as a function of frequency and voltage and use that as input to a finite element method (FEM) model to calculate the surface electric field and surface temperature. The surface temperature is possible to measure, thus used as a verification of the numerical model and to justify the calculated electric field.

3.1 Model simplifications

The main goal in this project is to compare how higher voltage frequencies (~10 kHz) influence the field grading properties of the end-winding with the design frequency of 50 Hz as a reference. Any increase in temperature or electric field can be calculated by FEM and experimentally verified by surface temperature imaging. It is therefore important to choose materials and geometries that are feasible to both model by FEM and create experimentally.

A generator bar has a rectangular cross section. This 3D geometry will add complexity to model in FEM software, thus a simplification to a 2D rotational symmetric geometry is used as seen in Figure 3-1. This simplification introduces some errors, as the non-rotational geometry is expected to introduce some hot spots with both temperature and high electric field. The simplification is, however, trying to match the curvature at the edges of the rectangular bar and thus simulate the highest electrical field.

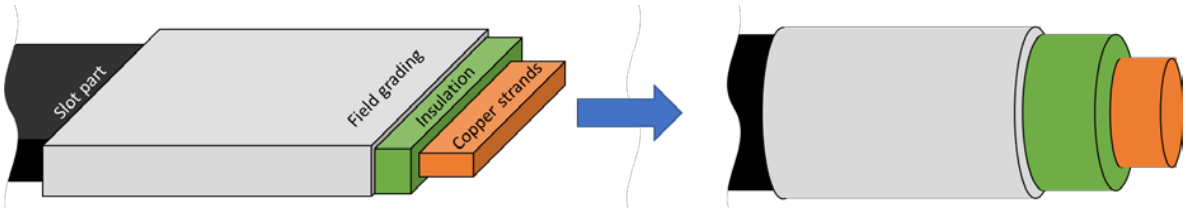

Figure 3-1: Sketch of a geometry simplification from rectangular bar cross section to circular test object cross section.

The field grading material can be applied as either a tape before the vacuum pressure impregnation process, or a resin rich tape or paint after curing of the insulation system. The field grading paint is expected to be isotropic in longitudinal and transversal direction, whereas the tape is a composite of field grading material backed on a supporting matrix, which results in anisotropic insulation system properties. The anisotropic insulation system means that the measured apparent conductivity and permittivity in transverse and longitudinal direction are different. The tapes are wrapped around the copper conductor, leading to a helix shape of the tape. One necessary simplification of the helix tape geometry is shown in Figure 3-2, where the detailed field grading tape geometry is simplified to an anisotropic and homogeneous material with different conductivity and permittivity in the longitudinal and radial directions, respectively.

For measurements of the conductivity and permittivity on this system, these are the resulting parameters.

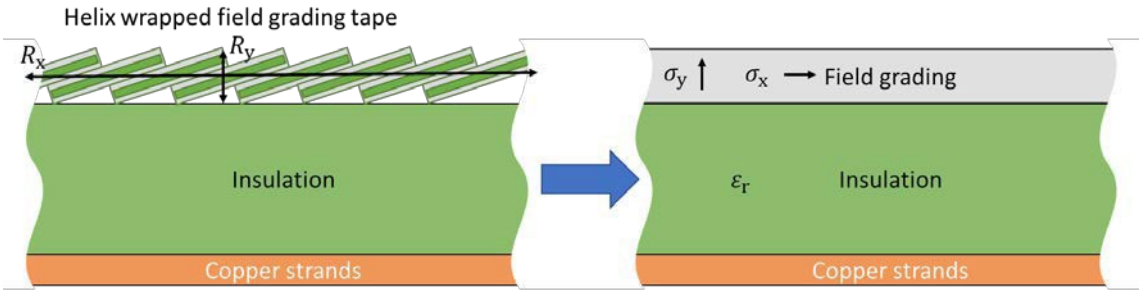

Figure 3-2: Sketch of a simplification of the field grading tape in helical geometry to a homogeneous anisotropic material, with similar properties as a field grading paint.

All test electrodes in this project are applied on top of the tested material. For highly non-linear materials, such as the field grading tape, this introduces some inaccuracies. Figure 3-3 sketches a probable *conducting volume* for different applied voltages, where the voltage in B is higher than in A. The de facto *conducting volume* in A is thus less than in B. The varying conducting volume originates from the non-linear behaviour of the material. A combination of current in longitudinal and transverse direction is jointly measured. It is therefore not necessary to measure the current in longitudinal and transverse direction separately, but it makes the calculated current density uncertain as the conducting cross section is not known. The uncertainty introduced by the limited conducting cross section is minimized by applying high electric fields, as it is more likely to include the complete field grading tape cross section to conduction.

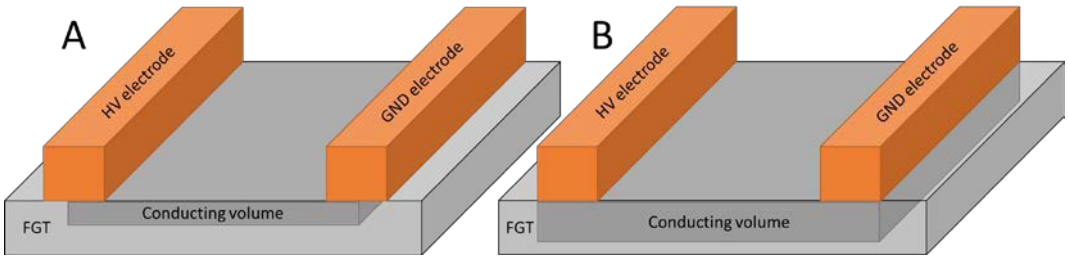

Figure 3-3**:** Sketch of assumed conducting volume for a low voltage (A) and high voltage (B). The non-linear conductivity limits the conducting volume when the voltage is low and utilizes the complete geometric volume when a high voltage is applied. The de facto *conducting volume* varies with applied electric field.

3.2 Test objects

The chosen model simplifications enable an easy use of field grading system, including a specific complex design geometry and different materials. This means that the chosen material systems are studied, rather than the pure material propertied. The following test objects have therefore been chosen:

T1. Test object T1 is sketched in Figure 3-4. and used for measuring the thermal conductivity of the materials. A sensor is sandwiched between two material samples with thickness 3 mm (FGT) or 6 mm (insulation) and area of 60 x 60 mm. The figure shows a cross-section of the test object, revealing the sensor sandwiched between the two disks.

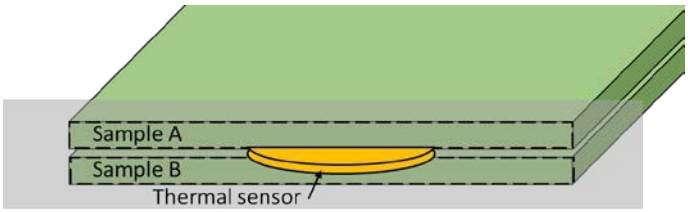

Figure 3-4: Cross section of Test object T1 for measuring of thermal conductivity

T2. Test object T2 is sketched in Figure 3-5 for measuring the capacitance of the materials, which enables calculations of the relative permittivity. Two half-overlapping layers are used with a total test object thickness of 0.4 mm. The HV electrode had a diameter of 30 mm.

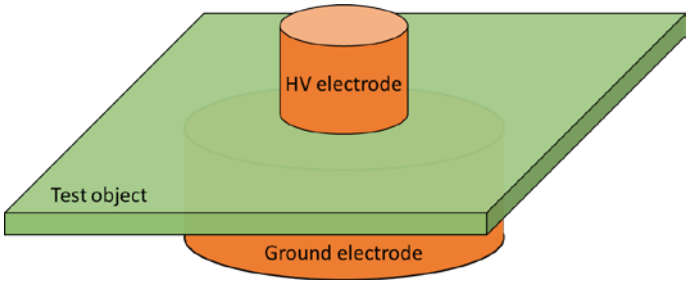

Figure 3-5: Test object T2 for measuring capacitance of the material.

T3. Test object T3, sketched in Figure 3-6, is used for measuring the longitudinal surface conductivity of the field grading system. The test object is created around a brass tube with diameter of 10 mm. An insulation layer of 3 mm thickness is then applied around and cured, creating a cylinder with diameter of 16 mm. A semi-conductive varnish (black), with high conductivity, is then applied to the middle part as OCP before the field grading tape is applied in a half-overlapping helix geometry for 20 cm with 2 cm overlap with the semi-conductive varnish. The voltage is applied between two copper tapes at the surface of the field grading system separated by 1 to 4 cm. The centre conductor is grounded, in which only surface currents, and near surface currents, are considered.

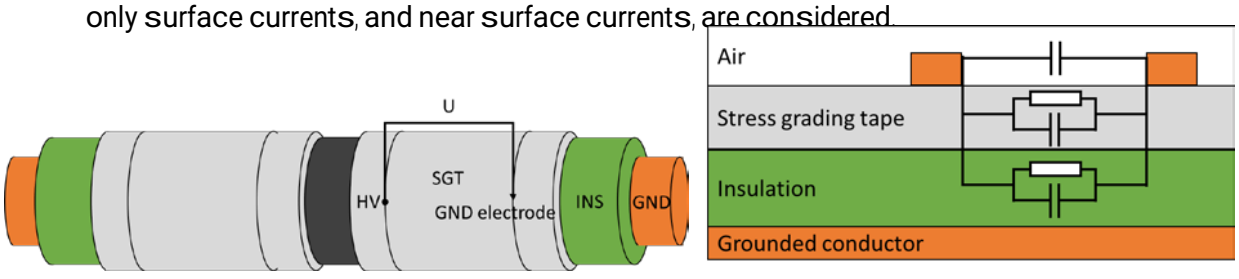

a) Sketch of the setup b) Equivalent circuit

Figure 3-6: Test object T3 for measuring of the longitudinal material properties. The ground (GND) electrode is connected to ground via an amperemeter.

T4. Test object T4 is obtained by modification of test object T3 in Figure 3-7 by applying the electrodes at different locations. The voltage is then applied as during normal service operation, between the semi-conductive layer and the centre conductor. The function of the field grading system is to create a termination and simulate a real stator bar.

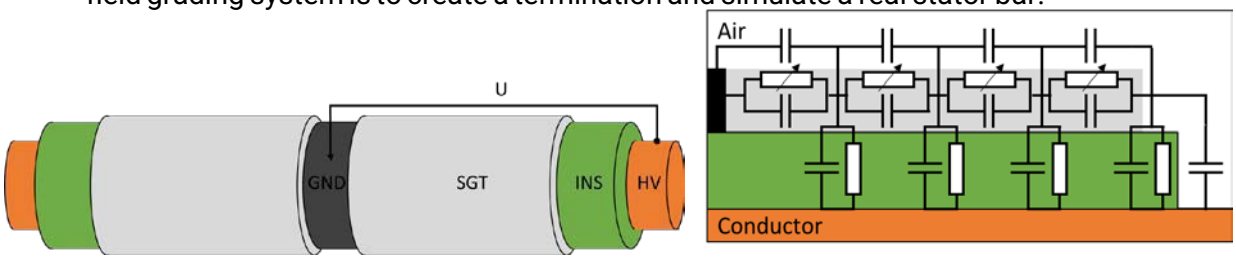

a) Sketch of the setup b) Equivalent circuit

Figure 3-7: Test object T4 for measuring on the complete system.

T5. Test objects T3 is created to measure the average of the field grading system including geometry and material properties. Test object T5 is therefore designed differently to measure material properties without the effect of the tape helix wrapping geometry. T5 is sketched in Figure 3-8**.** and consists of two layers of field grading tape, half overlapping before cured, in total 0.4 mm thick. The cured FGT sheet is placed on a mica/epoxy insulation sheet. A guarded electrode configuration is then placed on top of the field grading tape-paper. The width of the measuring electrode is 80 mm, whereas the electrode separation varies.

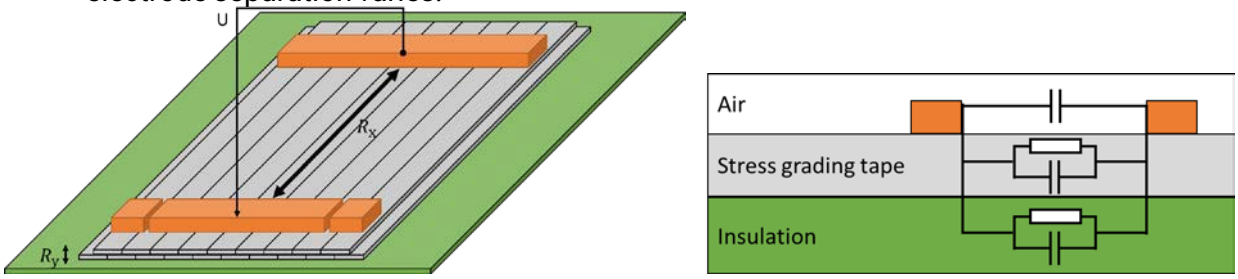

a) Sketch of the setup b) Equivalent circuit

Figure 3-8: Test object T5 for measuring material parameters in transverse direction at the surface

The chosen materials are tapes that are commercially available for use in hydropower stators. An overview is given in Table 3-1 Three field grading tapes, with strong, medium, and weak field grading properties, and one insulation tape as reference are studied. Additionally, a standard semiconductive varnish is used as OCP.

Table 3-1: Overview of the chosen field grading tapes, insulation tape, and semiconductive varnish.

Material		Tape width	Tape thickness	Thermal class	Label
Field grading tape	FGT A	20 mm	0.22 ± 0.03 mm	155 °C	Strong FGT
	FGT B				Medium FGT
	FGT C				Weak FGT
Insulation tape	Resin rich	40 mm	0.19 ± 0.03 mm		Insulation
Semiconductive varnish		Paint	Paint		OCP

3.3 Voltage and current model

A current through an object consists of a capacitive and resistive part. It is simple for a pure resistive object or a pure capacitive object as the other part can be neglected. However, for objects with a resistance and capacitance, or stray capacitances, it is not as simple to extract the capacitive and resistive current. Some mathematical relations are therefore presented here to enable the extraction of the resistive current to calculate the conductivity.

It is possible to represent any periodic voltage shape $u(t)$ by its Fourier series

$$u(t) = \sum_{k=1}^{\infty} U_k \cdot \sin(k\omega t) \tag{5}$$

where U_k is the amplitude of the k^{th} harmonic, and ω is the angular frequency. Similarly, the corresponding current signal $i(t)$ can be represented by its Fourier series

$$i(t) = \sum_{k=1}^{\infty} (a_k \cdot \cos(k\omega t) + b_k \cdot \sin(k\omega t)). \tag{6}$$

where the Fourier coefficients a_k, and b_k represents a parallel capacitance C_p and resistance R_p by

$$i(t) = i_R(t) + i_C(t) = \frac{u(t)}{R_p} + C_p \frac{du(t)}{dt} = \frac{1}{R_p} \sum_{k=1}^{\infty} U_k \sin(k\omega t) + C_p \omega \sum_{k=1}^{\infty} k U_k \cos(k\omega t) \tag{7}$$

It is thus possible to calculate the parallel series capacitance and resistance by comparing the Fourier components of the measured current to Equation (7).

The current density $jjjj$ and conductivity $\sigma\sigma\sigma\sigma$ are proportional by the electric field $EEEE$:

$$jjjj = \sigma\sigma\sigma\sigma EEEE \tag{8}$$

It is possible to deduce an apparent AC conductivity, which includes dielectric loss ε'' as

$$\sigma_{AC} = \sigma_{DC} + \varepsilon'' \varepsilon_0 \omega \tag{9}$$

In the model used in this work, the temperature dependence is assumed to follow an Arrhenius relationship for both the DC conductivity $\sigma\sigma\sigma\sigma_{DDDDAAAA}$, the imaginary part of the complex permittivity $\varepsilon\varepsilon\varepsilon\varepsilon''$, as a representation for the polarization mechanisms present, and ε_0 is the vacuum permittivity. The electric field dependence is assumed to simply follow an exponential function, which is a simplification of Equation (1) described in the literature review. This simplification is valid for the lowest electric fields. The DC conductivity is then described by

$$\sigma_{DDDDAAAA}(E, T) = A \cdot e^{B \cdot |E|} \cdot e^{-\frac{W_a}{k_B T}} \tag{10}$$

where A and B are constants, W_a is the activation energy, k_B is the Boltzmann constant, and T is the temperature in Kelvin. The constant $BBBB$ corresponds to the factor $mmmm$ in Equation (2), as $BBBB = mmmm \cdot \ln(10)$. Similarly, the dielectric loss is a function of electric field, temperature, and frequency with the parameters in a similar manner:

$$\varepsilon''(E, T, f) = \omega \cdot e^{B \cdot |E|} \cdot e^{-\frac{W_a}{k_B T}}. \tag{11}$$

These are empirical descriptions used as input to a FEM simulation. Also, other mathematical relations, such as $\propto \exp(\square \cdot \square)$, $\exp(\square \cdot \sqrt{\square})$, $\square^{\square}$, can be used to describe the measured conductivity satisfactory. The chosen empirical description is thus only valid in the measured region and cannot be used to predict the conductivity outside this region.

An electric field with a finite conductivity produces heat or has Joule losses. Joule losses is due to a current flowing through a resistance as

$$PPP = IIII^2 RRRR = \sigma\sigma\sigma\sigma \cdot VVVV \cdot EEEE^2, \quad (12)$$

where $PPPP$ is the power, $IIII$ is the current, $RRRR$ is the section resistance, $\sigma\sigma\sigma\sigma$ is the conductivity, $VVVV$ is the dielectric volume with current, and $EEEE$ is the electric field.

3.4 Experimental methodology

The methodology has three main goals for investigating the voltage frequency dependence ofthe electric field and heat production:

1. Measure material properties as input to FEM modelling
2. FEM modelling of electric field distribution and heat production
3. Measure surface temperature on the field grading system to verify the output of the FEM modelling

3.4.1 Thermal measurements

Measurements of the thermal conductivity are performed by use of a Thermal Constants Analyser TPS 2500 S (by HotDisk AB) using a sensor with radius 6.4 mm sandwiched between two flat disks described as Test object T1 illustrated in Figure 3-4.

3.4.2 Electrical characterization

The AC-conductivity of the field grading systems (geometry + materials) was measured on test object T3. The electrode separation was 10 mm to maximize the electric field with a limited voltage source. A sketch of the test system is shown in Figure 3-9. The voltage shape was generated by a function generator and amplified by a TREK 20/20C-HS. The voltage was measured by a Tektronix P6015A voltage probe. The current was amplified by a Standford Research 570 current pre-amplifier. The measured voltage and current were stored by a GaGe CS8347 computer-controlled oscilloscope. The test matrix is shown in Table 3-2. The permittivity could not be measured due to the influence of stray capacitances of unknown size.

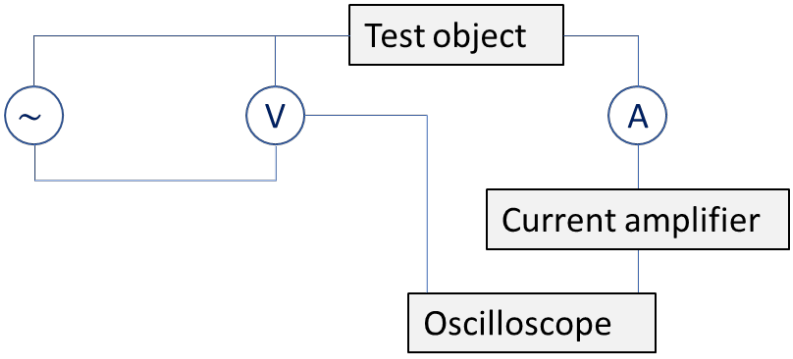

Figure 3-9: Schematics of the setup for measuring the conductivity and permittivity.

Table 3-2: Test matrix for measurements of longitudinal AC conductivity of the three FGT systems.

Parameter	Strong FGT	Medium FGT	Weak FGT
Electrode separation	10 mm - 40 mm	10 mm	10 mm
Maximum voltage	3.75 kV_{peak}	5 kV_{peak}	5 kV_{peak}
Temperature range	20 °C – 90 °C	20 °C – 90 °C	20 °C – 90 °C
Voltage frequency	1 Hz - 10 kHz	1 Hz - 10 kHz	1 Hz - 10 kHz

The voltage/current measurements were compared to dielectric spectroscopy using the IDAX 300 instrument at low voltage. IDAX 300 is, however, limited in voltage amplitude and frequency, thus only used as a reference for the other measurements. Test object T3 was used with an electrode separation of 4 cm and applied voltage peak of 200 V. The measured signals from IDAX and the voltage-current measurements gave similar results.

The bulk permittivity of the field grading materials was measured in test object T2 by an Agilent U1732A RLC-meter. It applies a low voltage in the range of 100 Hz - 10 kHz.

The longitudinal DC conductivity of the different tapes was measured in test object T5 by a Megger MIT525. The test parameters are shown in Table 3-3. The samples have a high conductivity; thus, the measured current stabilizes fast, and the DC resistance is therefore measured after only 60 s. The experiments was only performed on the field grading tapes, whereas values for the DC conductivity for the insulation was taken from (Aakre 2020).

Table 3-3: Test matrix for measuring of longitudinal DC conductivity of the three field grading tapes.

Parameter	Strong FGT	Medium FGT	Weak FGT
Electrode separation	0.5-8.5 mm	0.5-8.5 mm	0.5-8.5 mm
Voltage range	1-5 kV	1-5 kV	1-5 kV
Temperature range	20 °C – 90 °C	20 °C	20 °C

3.4.3 Surface temperature measurements

The current in the stator bar, and especially in the end-winding, create heat. The heat at the surface was measured by the fiber optical thermal sensor system Rugged Monitoring T301-08 connected to an Agilent Data logger on test object T5, thus mimicking the complete stator bar. A sketch of the surface temperature measurement is shown in Figure 3-10 where the 15 temperature sensors are evenly distributed with 1 cm separation distance + one sensor measuring the room temperature. The 4^{th} sensor is right above the semiconductive varnish end. A picture of the laboratory setup is given in Figure 3-11. The applied voltage was 5.5 kV_{peak}. The surface temperature stabilized after 10-15 min and one measurement at a selected frequency lasted typically 15 min.

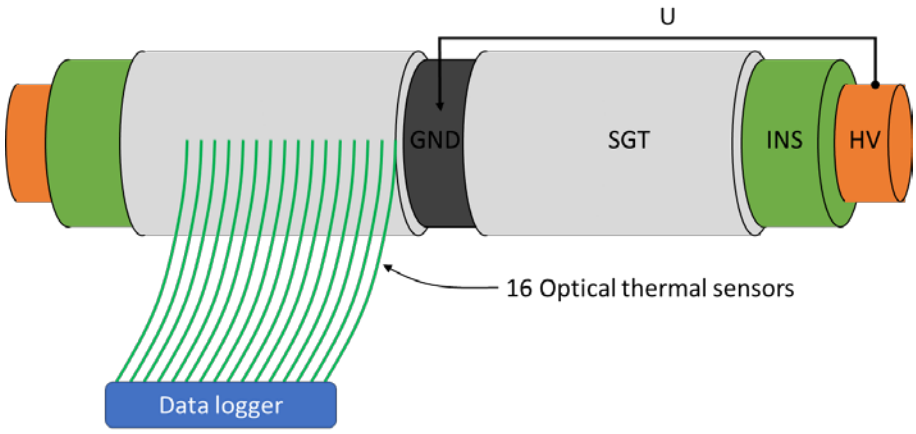

Figure 3-10: Sketch of setup for measuring the surface temperature with 16 equally distanced optical thermal sensors.

Figure 3-11: Picture of the measurement of surface temperature.

3.4.4 Finite element method simulation

Test object T4 was used as a model system for numerical finite element method simulations in COMSOL Multiphysics 5.6. The geometry is an axisymmetric 2D model, shown in Figure 3-12, where the different materials are indicated by different colours. The key dimensions are listed in Table 3-4 and are chosen to fit the experimental test object T4.

Table 3-4: Dimensions used in FEM simulations.

	Dimension [mm]
Thickness of insulation	3
Thickness of OCP	0.4
Thickness of FGT	0.4
Distance from slot to FGT	20
Overlap between FGT and OCP	20

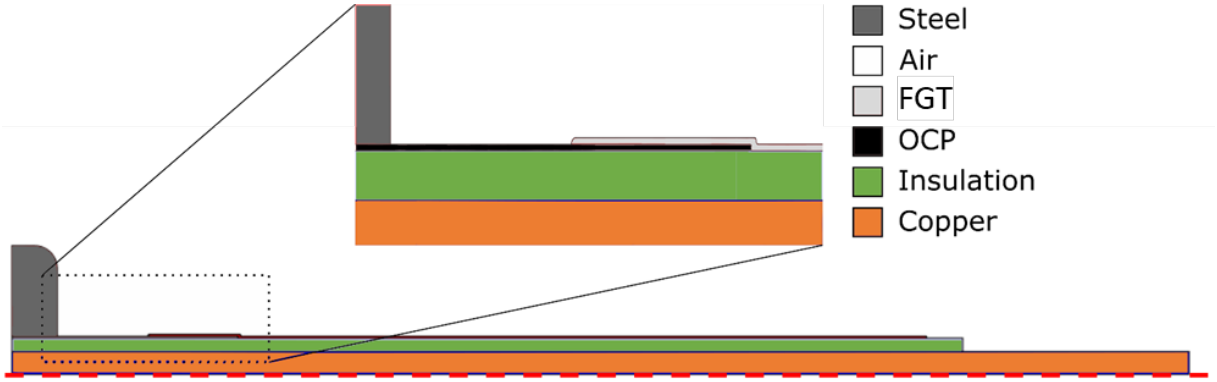

Figure 3-12: Illustration of full geometry used in FEM simulations. Details of the overlap between the OCP and FGT are shown in the inset. The colours denote the different materials in this model. The red dashed line on the bottom is the axis of rotational symmetry.

The material properties used in the simulations are listed in Table 3-5. Values for electrical conductivity, relative permittivity, and thermal conductivity for the FGT and insulation are obtained in this work, and the table therefore reference to the result section from the experimental part. The important values for the OCP are the conductivity and permittivity. The thermal properties are less important. The COMSOL model includes the heat capacity, but a parameter sweep shows that there is no difference in the surface temperature if the value of the heat capacity is 500, 1000 or 3000 J/(kg·K). A figure describing this is shown in Figure A-3 in the appendix.

Table 3-5: Values for material parameters used in simulations. The asterisks denote values obtained inthe experimental work presented later in this report.

	Steel[1]	Copper[1]	Air[2]	FGT	Insulation	OCP
Electrical conductivity [S/m]	$4.032 \cdot 10^{6}$	$5.998 \cdot 10^{7}$	$1 \cdot 10^{-17}$	*	*	*
Relative permittivity	1	1	1	**	**	**
Density [kg/m^3]	7850	8960	N/A[5]	1800(4)	1300(4)	1200(4)
Thermal conductivity [W/(m^2·K)]	44.5	400	N/A[5]	***	***	***

[1] Standard COMSOL values, [2] COMSOL solution to electrical conductivity = 0 S/m to avoid numerical problems, [4] Calculated from datasheets, [5] The heat transfer coefficient is used instead, * see Equation (13) and Table 4-4, ** see Table 4-2, *** see Table 4-1.

The boundary conditions are a sinusoidal voltage of frequency f and amplitude V_a is applied to the copper, and the steel is grounded. The thermal boundary condition is natural heat convection on the interface between the solid materials and air. As there is no forced air circulation in the laboratory where experiments were performed, the heat transfer coefficient h is set to 20 W/m^{2}K (Y.A. Cengel, n.d.). The ambient temperature is 20 °C. This means that the thermal properties of air are unimportant and not used as the heat transfer coefficient is describing the mechanism better.

The electric time scale is much shorter than the thermal time scale. The lowest frequency of the electric field is 50 Hz meaning that the electrical time scale is 20 ms, whereas it takes many minutes to notice any temperature change. It would require too much computational time to simulate both electric and thermal physics at the same time since very short time steps are

required for the electric field. Therefore, the simulations are performed in two steps. First, the stationary solution for the electric field is calculated. This is used as the input for the second step where the thermal part is solved. These two steps are solved for each combination of voltage frequency and amplitude. Splitting the simulation into two parts removes the effect of the temperature increase on the electrical conductivity. However, the temperature dependence on the electrical conductivity is very small, and therefore considered insignificant here.

4 Results

4.1 Thermal conductivity

The measured thermal conductivity for the three FGTs and the insulation as a function of temperature is shown in Figure 4-1. The average values are shown in Table 4-1. There is no significant temperature dependence, and the thermal conductivity increases with the strength of the FGT. That can indicate that a higher concentration of SiC increases thermal conductivity.

An attempt was made to measure the thermal conductivity of the dried OCP varnish; however, it was not possible to create sufficiently thick samples to successfully measure due to high thermal conductivity. A parameter sweep in COMSOL showed that there is a negligible influence of the thermal conductivity of the OCP-varnish, as seen in Figure A-4 and Figure A-5. A standard value based on literature was therefore chosen as given in Table 4-1

Table 4-1: Average value of measured thermal conductivity for the involved materials.

Temperature °C	Insulation W/(m·K)	Weak FGT W/(m·K)	Medium FGT W/(m·K)	Strong FGT W/(m·K)	OCP W/(m·K)
40	0.503	0.856	0.990	1.034	-
60	0.509	0.866	0.978	1.041	-
90	0.554	0.886	1.000	1.011	-
Average	0.522	0.869	0.989	1.029	0.46

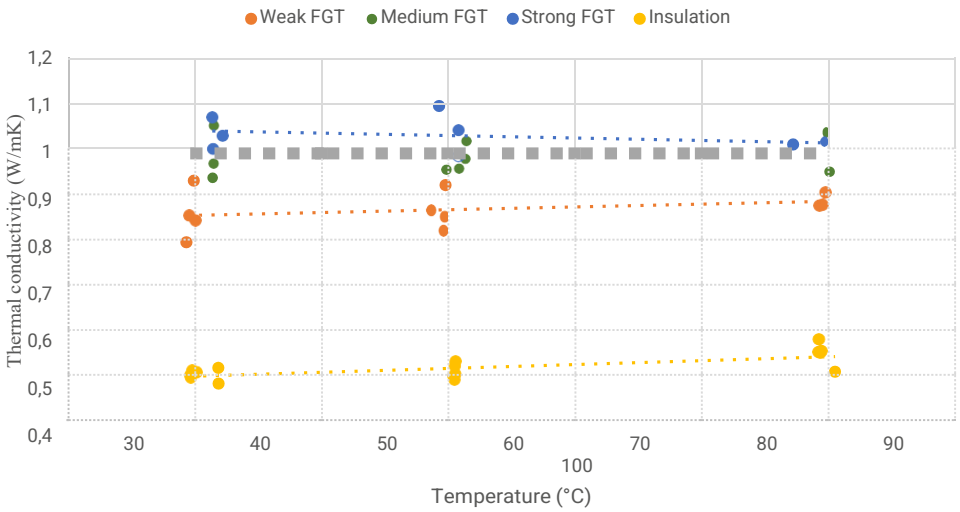

Figure 4-1: Measured thermal conductivity as a function of temperature, with a linear trendline added.

4.2 High frequency permittivity

Measurements of the high frequency permittivity were performed using the RLC meter on the three FGTs formed as test object T2 with a thickness of 0.4 mm and smooth surface. The set-up had a measured geometric capacitance of C_0 = 15.6 pF. The measured capacitance of the test objects and calculated relative permittivity given in Table 4-2 show that both parameters decrease with increased strength of the FGT.

The measured permittivity is highly dependent on the sample thickness and a high conductivity can trouble the accuracy of the results. If the conductivity is high, then the apparent sample thickness is reduced, thus reducing the relative permittivity by the same factor. A cylindrical object of the OCP varnish was also tried to be tested, but the high conductivity made it impossible to get a value. A parameter sweep of the relative permittivity of the OCP, Figure A-1 and Figure A-2, showed no influence between values of 1 and 1000, thus, this parameter was not investigated further.

Table 4-2: Measured FGT capacitance with corresponding calculated relative permittivity. The high conductivity of the FGTs makes the relative permittivity calculations inaccurate due to an unknown apparent sample thickness as the conductivity de facto short-circuit parts of the sample.

	Capacitance C	Relative permittivity ε_r
Strong FGT	100 pF	6.4
Medium FGT	110 pF	7.0
Weak FGT	120 pF	7.7
Insulation		4.4*
Dried OCP varnish		1**

*From (Aakre 2020) ** Not possible to measure nor relevant for the model

4.3 Current measurements

Results from current measurements on test object T3 are presented in this section. One period of a voltage cycle with measured voltage and current at 40 °C is shown in Table 4-3 for the three FGT at the given voltage frequencies with applied voltage of 3.75 kV_{peak} (375 V/mm). Voltage and current curve shapes were similar at all investigated temperatures (20 °C to 90 °C). The measured current for the strong FGT is almost purely resistive at 50 Hz (in phase with the voltage). The magnitude of the conductivity determines at which frequency the capacitive current starts to dominate. The difference between the FGTs is visible at 1 kHz, where the strong FGT is still almost purely resistive, whereas the medium FGT and weak FGT are dominated by the capacitive current. The capacitive current is dominant for all FGTs at 10 kHz. Spikes in the current at 1 Hz and 50 Hz originate in PD activity.

Table 4-3: Measured sinusoidal voltage (orange) and current (blue) for one voltage cycle at the given frequencies, measured at 40 °C. The measured current is mathematically decomposed in capacitive (red) and resistive (green) current. The capacitive current is proportional to the derivative of the voltage, whereas the resistive is the remainder.

	Strong FGT	Medium FGT	Weak FGT
1 Hz	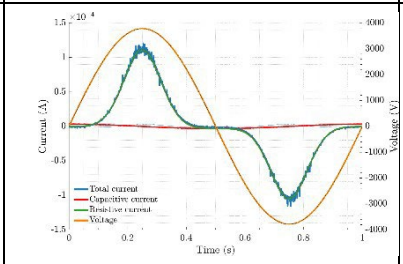	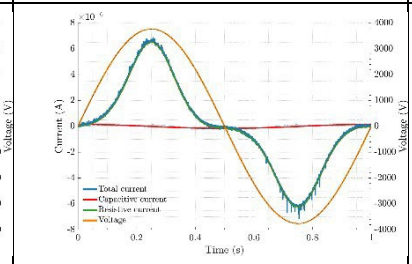	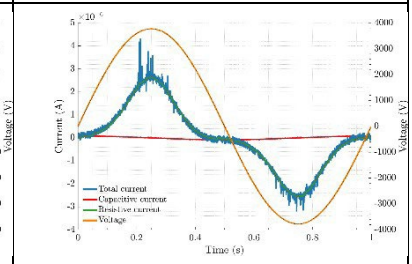
50 Hz	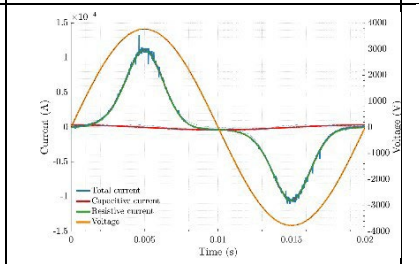	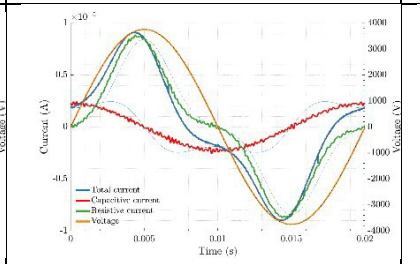	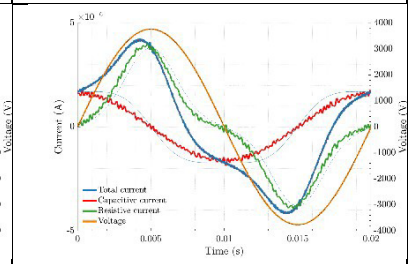
1 kHz	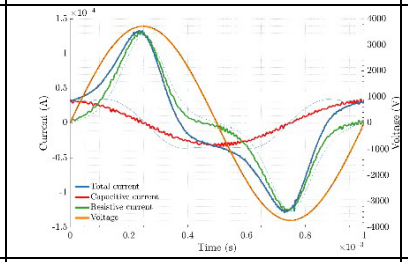	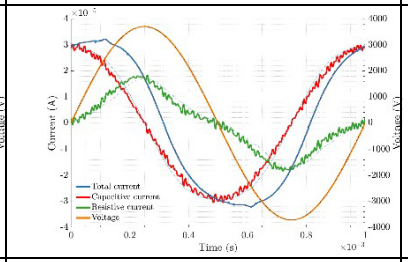	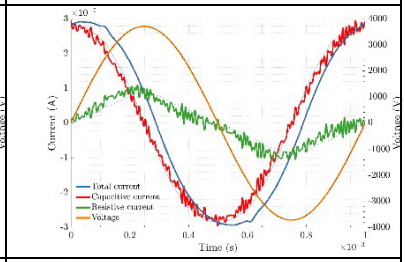
10 kHz	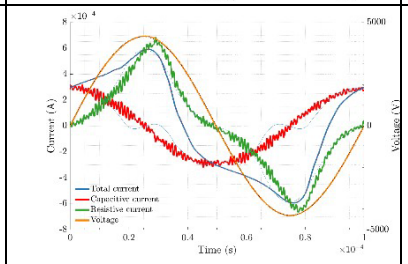	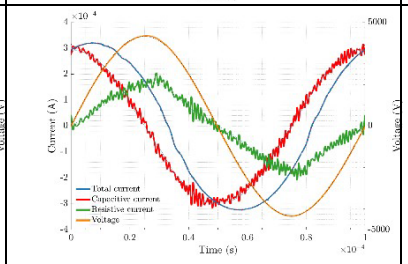	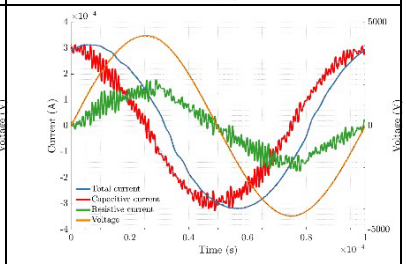

The measured current for strong FGT from Table 4-3 at 50 Hz and 10 kHz is presented as a function of applied voltage in Figure 4-2 and Figure 4-3, respectively. These figures clearly compare the measured current (blue) to the decomposed capacitive current (dotted black line) and resistive current (black line). The resistive current strongly dominates at 50 Hz with a minor contribution from the capacitive part. At 10 kHz, the two current contributions are comparable, but the capacitive part is slightly higher. Only the resistive part is used in the further examination due to elements of uncertainty introduced by unavoidable and unknown stray capacitances and the object capacitance itself.

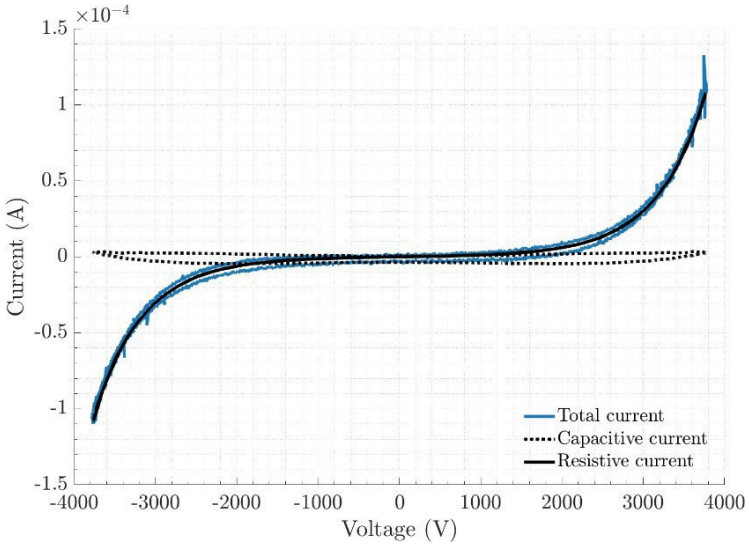

Figure 4-2: Measured total current as a function of applied voltage at 50 Hz for strong FGT at 40 °C. The current is also decomposed to the resistive and capacitive part.

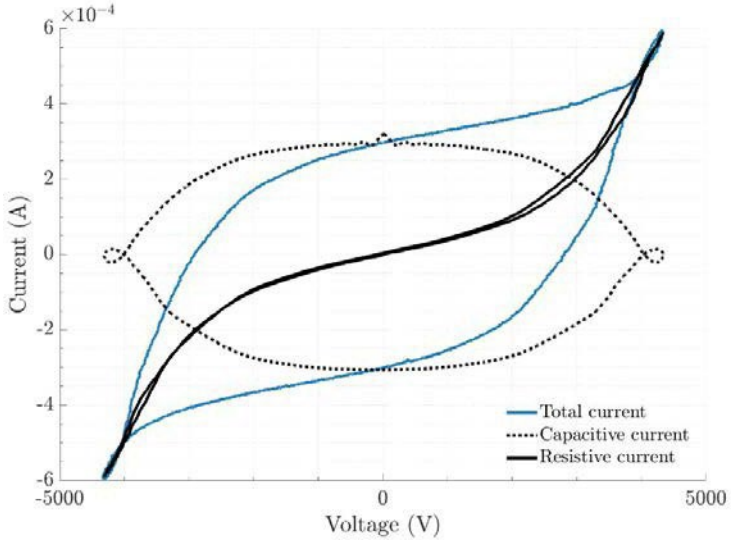

Figure 4-3: Measured total current as a function of applied voltage at 10 kHz for strong FGT at 40 °C. The current is also decomposed to the resistive and capacitive part.

4.4 AC conductivity

The AC conductivity is calculated from the resistive part of the measured current from test object T3, as shown in Table 4-3. The current was first normalized to current density by dividing by the conducting cross section before being separated in a resistive and a capacitive part. The resistive current density j_R was used to calculate the conductivity as $\sigma = j_R/E$. The AC conductivity is described by combining Equations (9), (10), and (11):

$$\sigma = A \cdot e^{B\sqrt{E}-\frac{a\sigma}{B}} + \sigma_0 \cdot \omega \cdot e^{-\frac{a\varepsilon}{B}} \quad (13)$$

The resistive part of the measured current presented in Table 4-3 was curve fitted to Equation (13) for all frequencies and temperatures in one fit for each of the three different FGTs. The parameters are shown in Table 4-4. The low voltage DC conductivity is equal for the three FGTs, and 6 orders of magnitude higher than the insulation. The difference between the three FGTs is in their field and frequency dependence.

The measurements for OCP were performed by a multimeter on test object T3 before applying FGT to ensure a low resistance in a simple way. No detailed measurement was performed, as the purpose of the OCP was to have a high conductivity to not influence the electric field distribution in the FGT. The measured resistance of the object was 5 kΩ, where the electrode separation was 100 mm, and the thickness of the OCP layer was 0.5 mm on top of an insulated brass tube with diameter of 17 mm. The conductivity of the OCP was therefore calculated to be approximately 1 S/m.

Table 4-4: Curve fitted parameters for the three FGTs to Equation (13). The DC conductivity σ_{DC} at low voltage is shown for easier comparison of values.

	σ_{DC} (S/m)	A (S/m)	B ($m^{1/2}/V^{1/2}$)	$W_{a,\sigma}$ (eV)	C (-)	$W_{a,\varepsilon}$ (eV)
Strong FGT	$1.2 \cdot 10^{-9}$	$1.15 \cdot 10^{-9}$	$1.52 \cdot 10^{-2}$	0.0007	$1.29 \cdot 10^{2}$	$2.62 \cdot 10^{-2}$
Medium FGT	$1.0 \cdot 10^{-9}$	$1.71 \cdot 10^{-8}$	$1.12 \cdot 10^{-2}$	0.072	$3.53 \cdot 10^{1}$	$1.24 \cdot 10^{-2}$
Weak FGT	$2.6 \cdot 10^{-9}$	$4.54 \cdot 10^{-8}$	$0.80 \cdot 10^{-2}$	0.077	$5.45 \cdot 10^{1}$	$2.44 \cdot 10^{-2}$
OCP	1	-	-	-	-	-
Insulation*	$5.0 \cdot 10^{-15}$	$1.85 \cdot 10^{-7}$	0	0.440	0	0

* Based on data from (Aakre 2020)

The calculated conductivity as a function of electric field with an amplitude of 375 V/mm is shown in Figure 4-4, and as a function of frequency in Figure 4-5, for the three FGTs together with the model in Equation (13). Only results from 40 °C are shown, as there is hardly any temperature dependence. The measured current close to 0 V/mm is small, thus the conductivity is calculated based on 0 divided by 0, which means that a small noise signal is expected to be amplified.

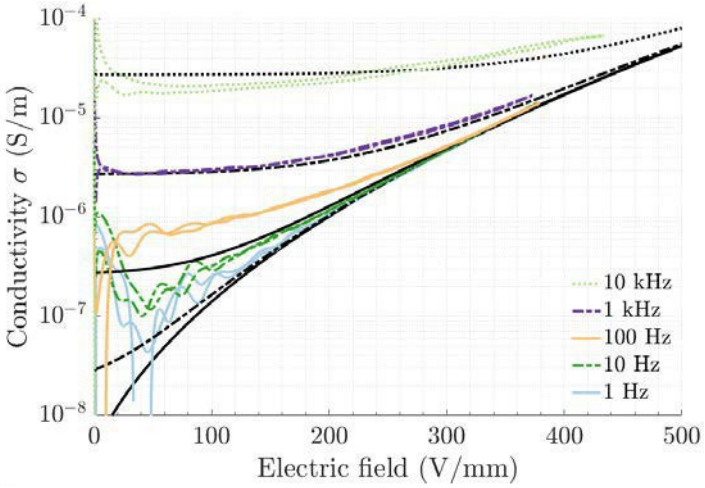

a) Strong FGT

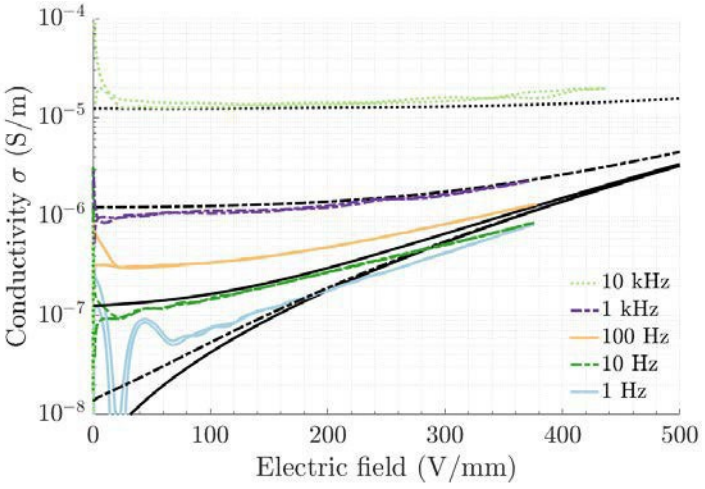

b) Medium FGT

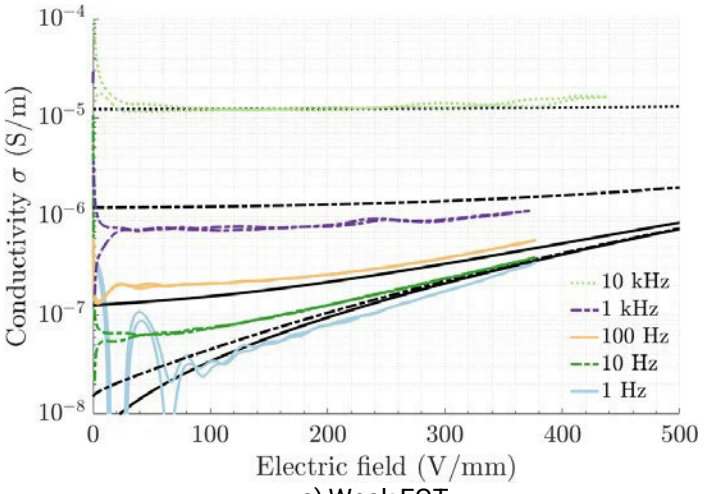

c) Weak FGT

Figure 4-4: Calculated conductivity as a function of electric field at indicated voltage frequencies (coloured lines). The model in Equation (13) is shown as black lines with the same line shape. The presented measurements were performed at 40 °C, but all temperatures were included in the curve-fitting.

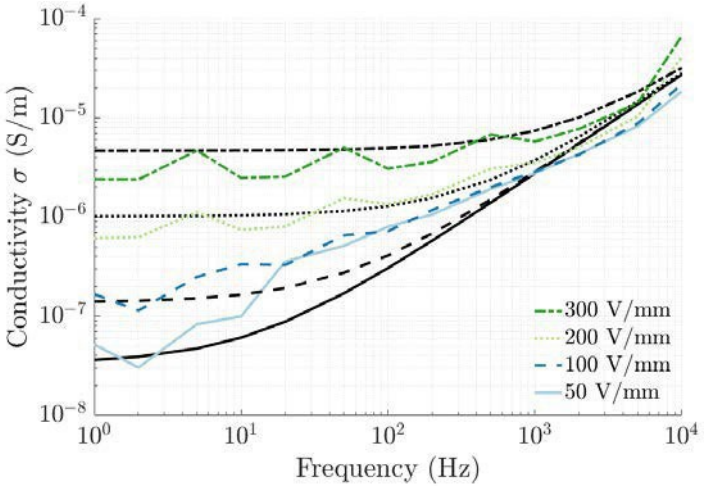

a) Strong FGT

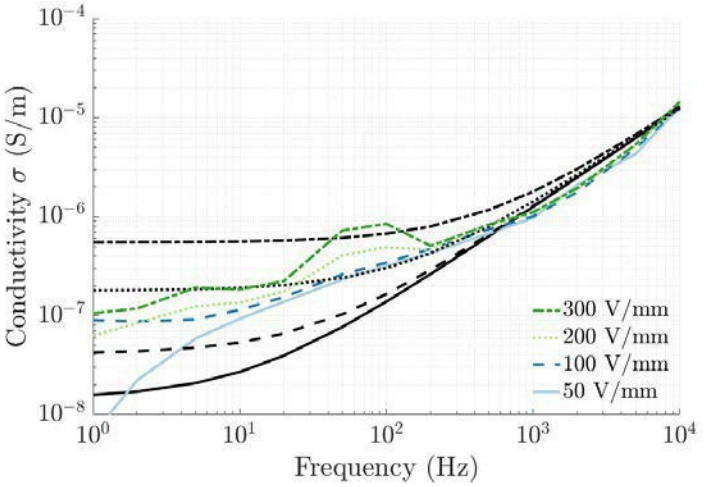

b) Medium FGT

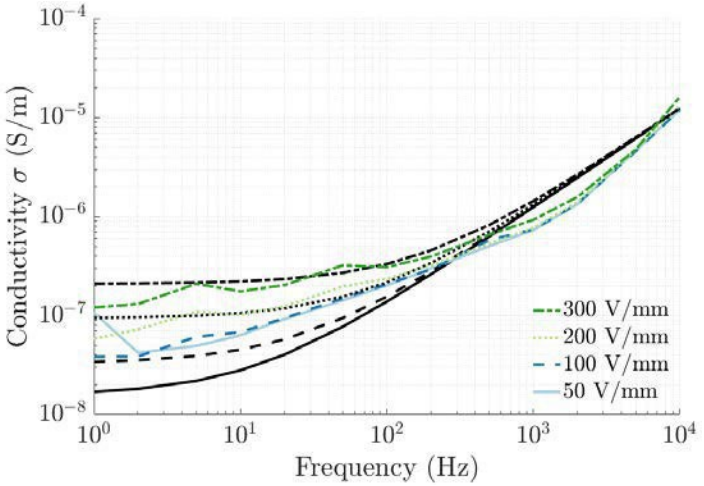

c) Weak FGT

Figure 4-5: Calculated conductivity as a function of applied voltage frequency at electric field amplitudes (coloured lines). The model in Equation (13) is shown as black lines with the same line shape. The presented measurements were performed at 40 °C, but all temperatures were included in the curve-fitting.

4.5 DC conductivity

The measured electric DC conductivity *along the FGT* ($\sigma\sigma\sigma\sigma_{xxxx}$) as a function of applied electric field is shown in Figure 4-6. The test object is different from what was used measuring the AC conductivity, thus a higher conductivity is expected. The curve fitted numbers are shown in Table 4-5 together with the corresponding values from the AC curve fitting with ω=0. The field dependence is comparable for all FGTs; however, the absolute value is smaller from the AC case. This can be a result of small, measured numbers at low fields for AC, and are thus inaccurate. Additionally, it is expected that the conductivity of the DC case is higher due to a geometry that facilitates the conductivity slightly more than the object used for the AC case, thus providing a plausible explanation of the difference between AC and DC.

Table 4-5: Curve fitted parameters for the three FGTs to Equation (13) at 20 °C when $WWW_{xxx,yyy} = 2222$ and $\omega\omega\omega\omega = 2222$. The values for *A* and *B* from AC measurements are obtained when $\omega\omega\omega\omega = 2222$.

	A from DC	*B* from DC	*A* from AC	*B* from AC
Strong FGT	$5.64 \cdot 10^{-9}$	0.017	$1.2 \cdot 10^{-9}$	0.015
Medium FGT	$7.68 \cdot 10^{-9}$	0.011	$1.0 \cdot 10^{-9}$	0.011
Weak FGT	$2.78 \cdot 10^{-9}$	0.011	$2.6 \cdot 10^{-9}$	0.008

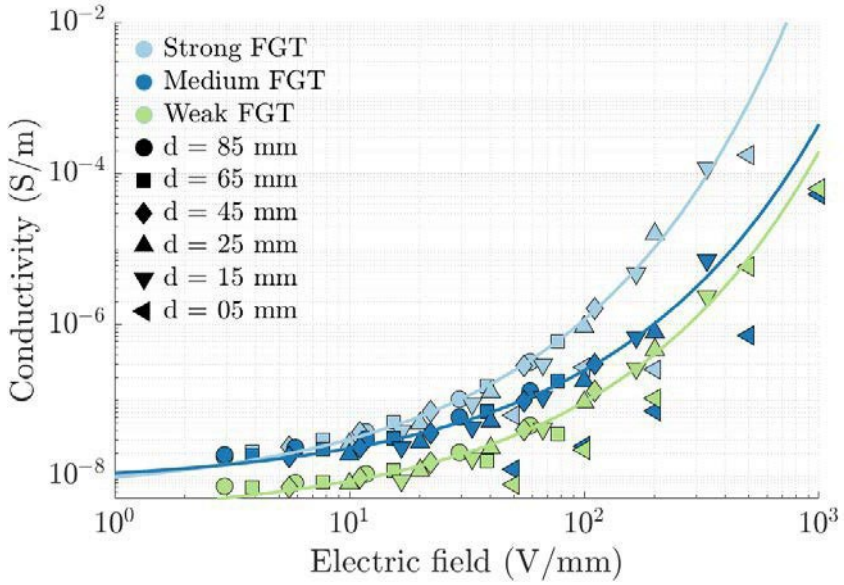

Figure 4-6: Measured DC conductivity as a function of applied electric field measured at 20 °C. The tests were done at the three FGTs at test object T5 with at Megger.

The measured conductivity as a function of electric field at different temperatures for the strong FGT are shown in Figure 4-7. The temperature dependence is present, which is not the case for the helix wrapped geometry and the strong FGT. This can also mean that the temperature dependence is most prominent at the DC case.

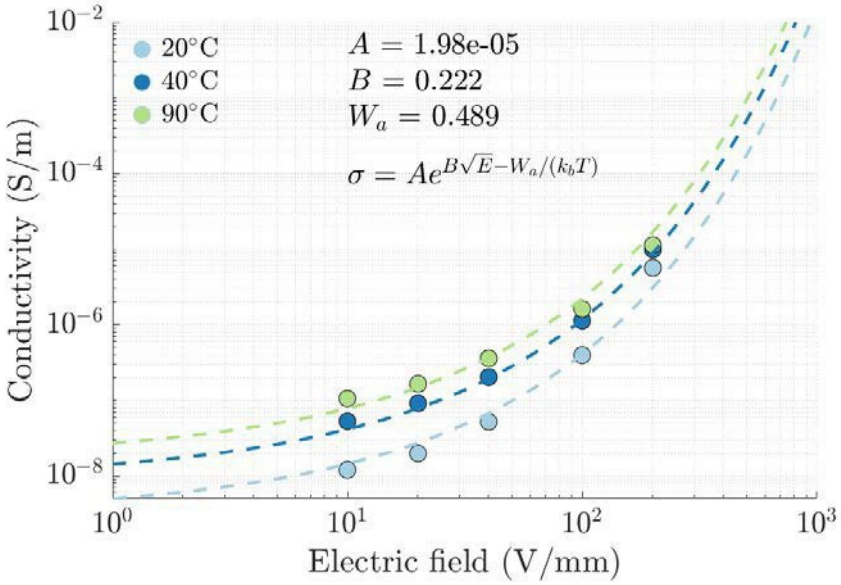

Figure 4-7: Measured DC conductivity as a function of applied electric field at the indicated temperatures. The tests were done at the strong FGT at test object T5 with two layers (thickness = 0.4 mm) with a Megger.

4.6 Surface thermal mapping

The maximum measured and simulated surface temperature at test object T4 is shown as a function of applied frequency in Figure 4-8 for the weak and strong FGT. The applied voltage was 5.5 kV_{peak}. The maximum surface temperature occurs at the end of the semi-conductive OCP. An almost linear surface temperature increase with frequency is observed. The trends were identical for both measured and simulated values.

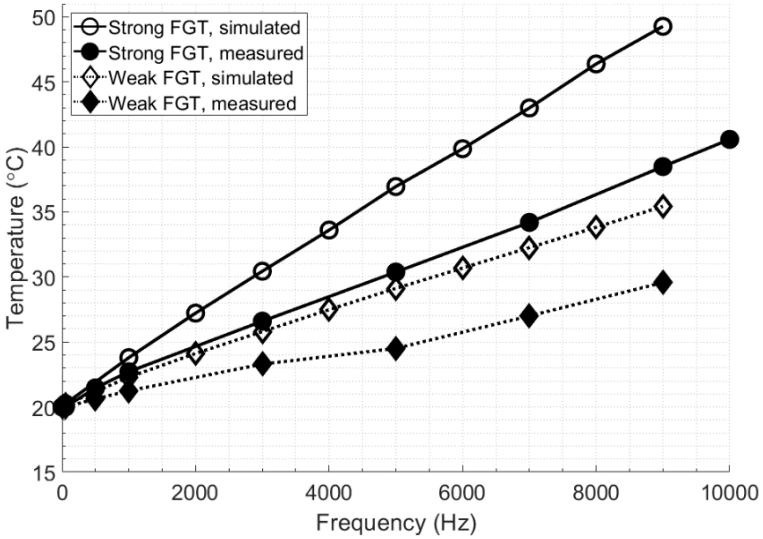

Figure 4-8: Measured and simulated peak surface temperature at the FGT as a function applied voltage frequency at the end of the OCP. The applied peak voltage was 5.5 kV.

The spatial dependence is given as a direct comparison of simulated and measured surface temperature is given in Figure 4-9 for the three FGTs in a-c. The overall similarity between the measured and simulated surface temperature is good. The frequency dependences are almost the same, but the absolute values differ. The absolute values of the measured temperatures are uncertain, as the exact thickness of the test object was not uniform. Producing samples with uniform radius was challenging, hence the thickness of the insulation varied somewhat along the test object. The differences might also be caused by low conductivity in the OCP at higher frequencies. In any case, the model provides an accurate representation of the main trends as a function of frequency and spatial distribution.

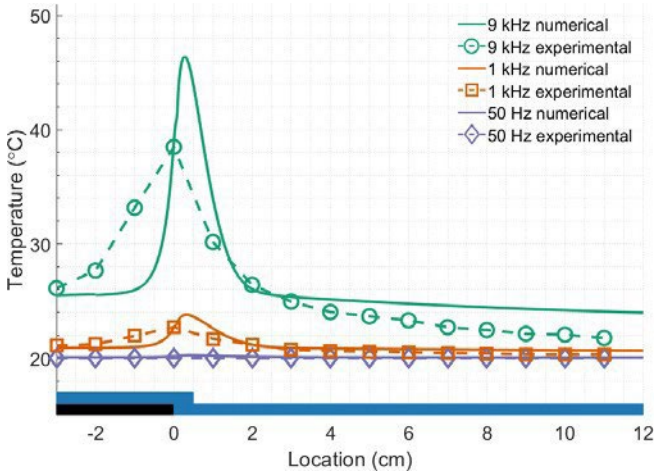

a) Strong FGT

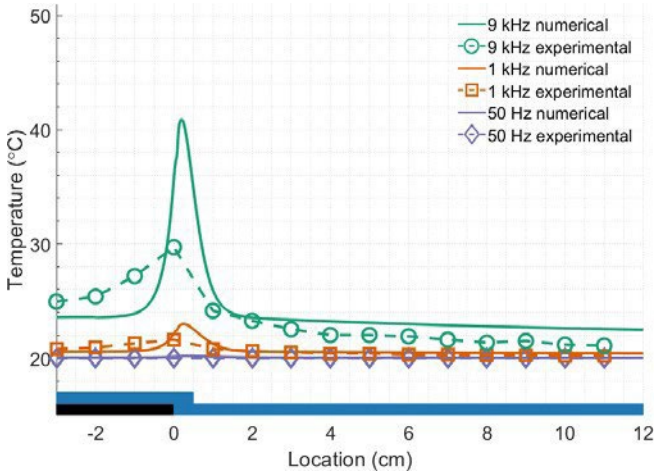

b) Medium FGT

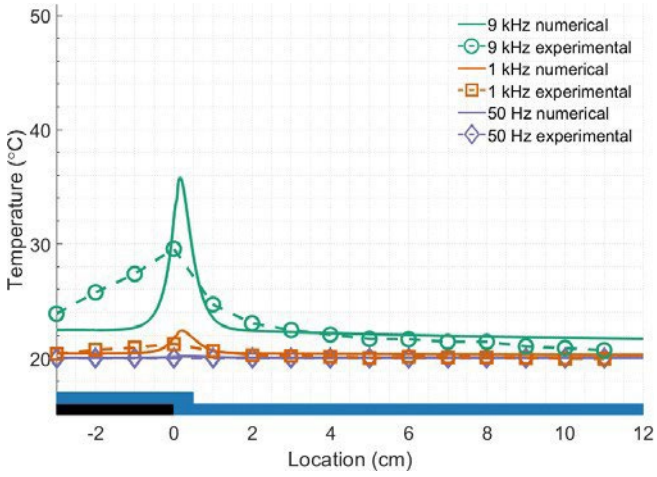

c) Weak FGT

Figure 4-9: Comparison of experimentally measured and numerically obtained surface temperature.

4.7 Surface electric field

The electric field in the cross section around the end of the OCP of a sample with strong FGT is shown in Figure 4-10 for both 50 Hz in a) and 9 kHz in b). It is seen that the electric field inside the FGT is fairly even, and any field enhancements occur in the air or in the insulation. The high electric field in the insulation is below breakdown, as this is a material with high withstand strength. The high electric field in the air might be more problematic as surface discharges might occur. The electric field is at 9 kHz concentrated more to the end of the OCP, thus, a higher electric field is seen. The electric field inside all strengths of FGT is summarized in Figure 4-11. The maximum electric field is 1.4 kV/mm, obtained at 9 kHz for the Weak FGT. This means that the electric field is outside the range where conductivity was measured. This rises some uncertainty to the accuracy of the calculations.

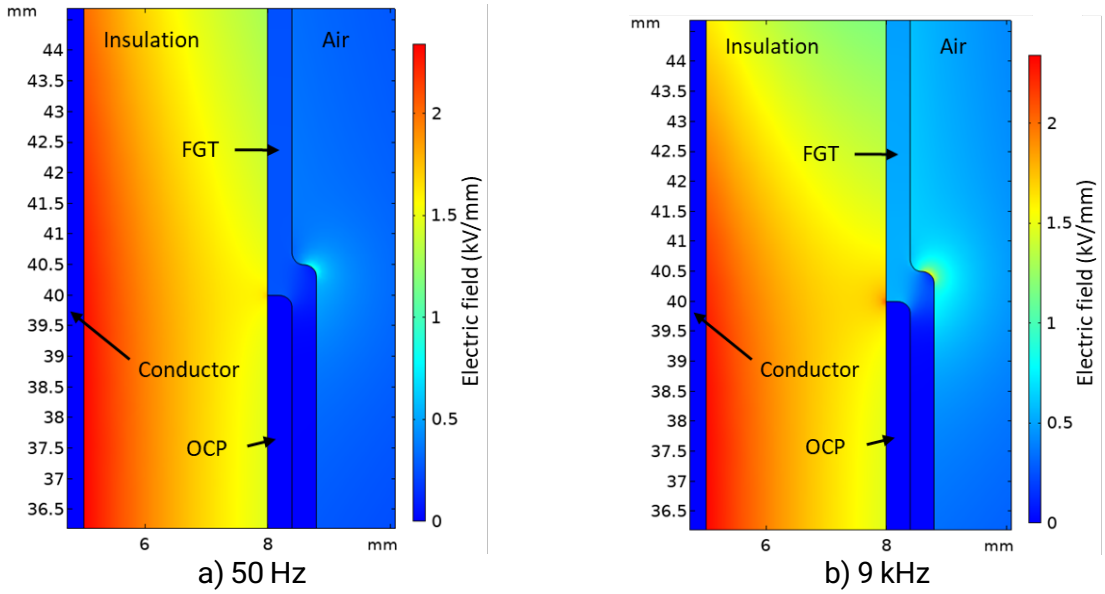

Figure 4-10: Electric field distribution around the end of the semi-conductive varnish with the strong FGT. The applied peak voltage is 5.5 kV.

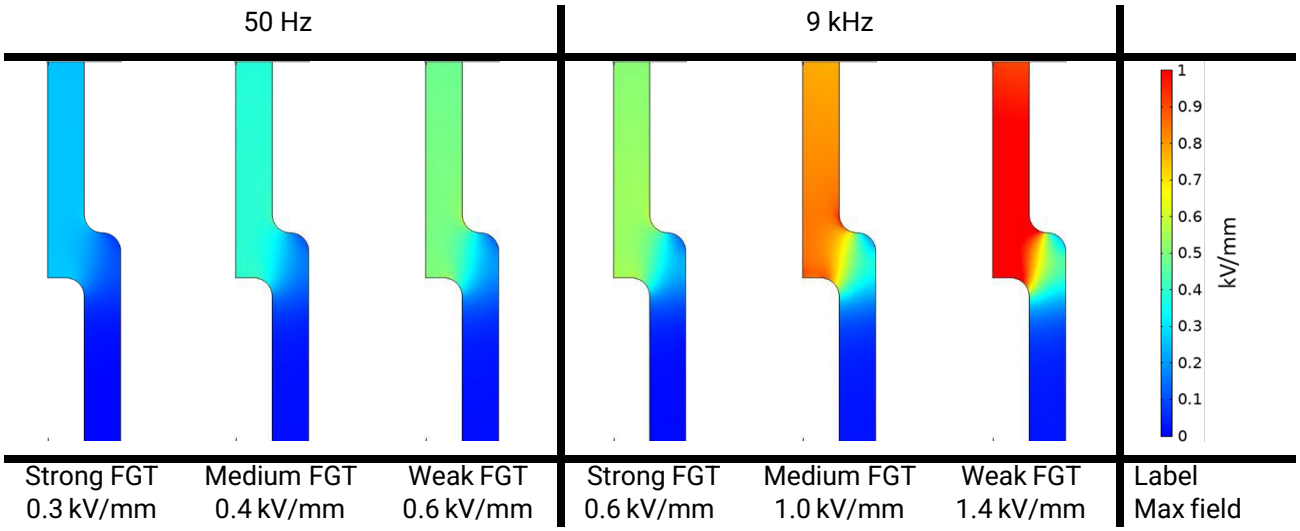

Figure 4-11: Electric field inside the FGT at indicated FGTs and frequencies.

The surface electric field was measured 0.1 mm above the FGT surface and is shown in Figure 4-12. The main observations are that the strong FGT is grading the electric field best, and that the field grading is worst at 9 kHz.

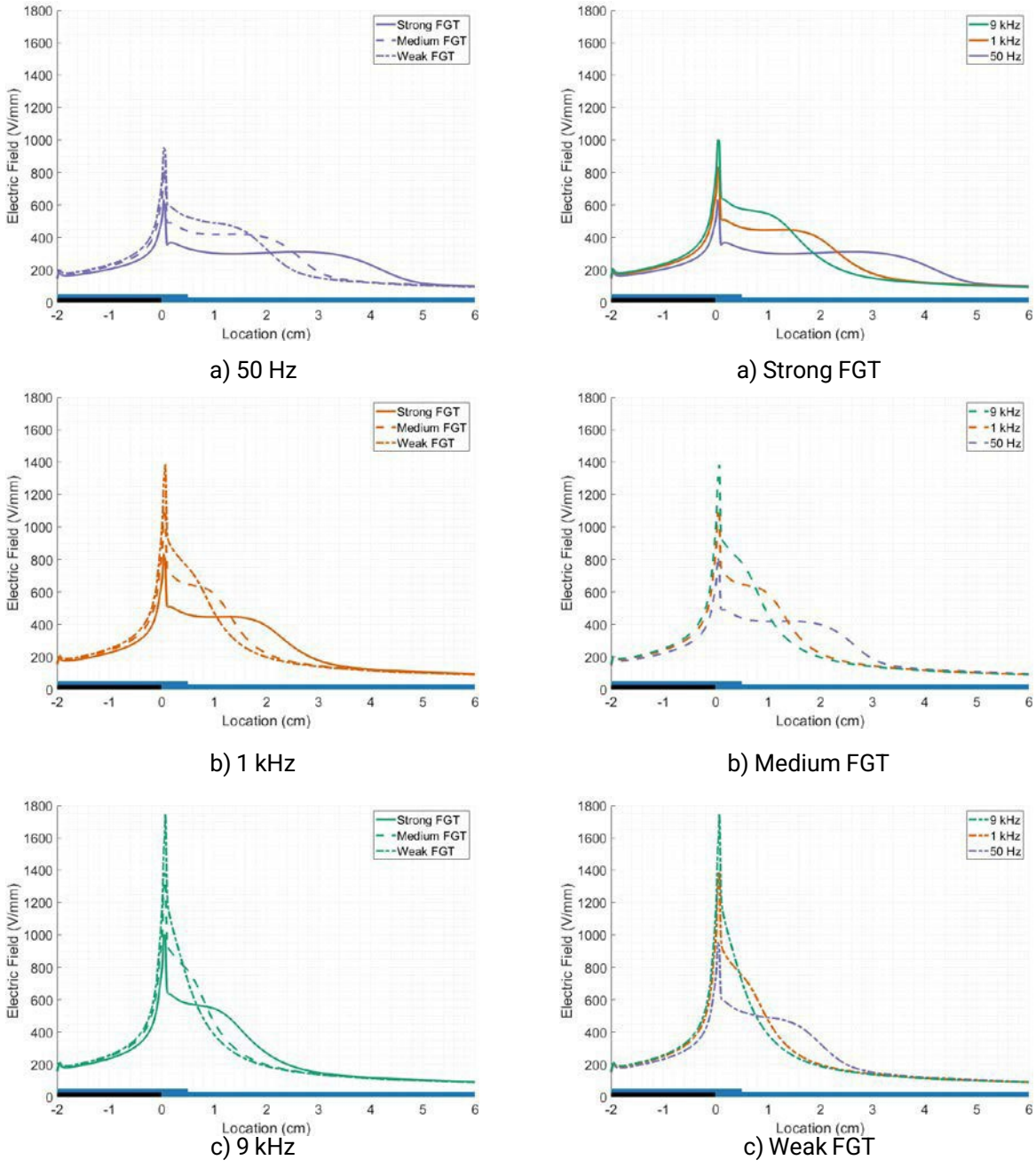

Figure 4-12: Simulated electric field as a function of spatial location relative to the end of the semi-conductive varnish (black) for the three FGTs. The applied peak voltage was 5.5 kV. (No, there is no mistake that the figures are almost similar in horizontal comparison)

The maximum electric field at the surface of the FGT is influenced by the curvature of the end of the OCP. This geometry is not known in practical applications; thus, only approximate values can be obtained. It is therefore necessary to use another parameter to describe the electric field shape. One option is to use the width of the electric field distribution as a measure on how effective the field grading is. A definition of the peak width is described in Figure 4-13. Here, the peak is defined as the stable plateau from the end of the OCP at 0. The peak width is not a perfect measure; however, it indicates the overall trend, making it possible to compare different field grading curves. The inverse of the peak width is almost proportional to the average surface electric field. A summary of the peak width as a function of frequency for the three FGTs are given in Figure 4-14. It is seen that the peak width quickly reduces with increasing frequency. This means that the field grading becomes ineffective at relatively low frequencies, such as 1 kHz. The peak width is larger for the strong FGT than the weak FGT, meaning that the strong FGT is better in grading the electric field.

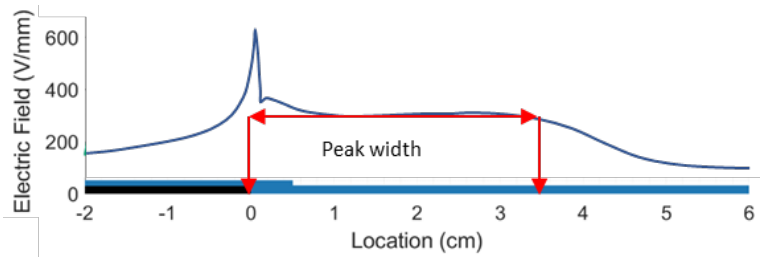

Figure 4-13: Definition of electric field peak width. The peak width is defined as the surface length with a flat plateau as indicated and until the cut-off of that plateau.

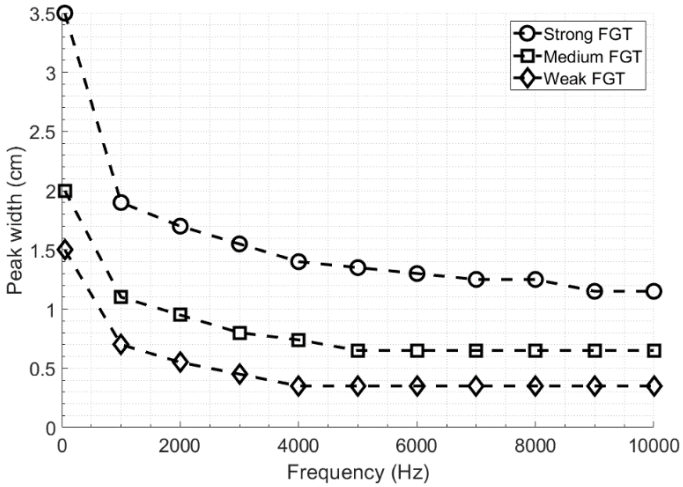

Figure 4-14: Spatial peak width of the electric field relative to the end of the semi-conductive varnish as a function of voltage frequency. The applied peak voltage was 5.5 kV.

4.8 Impact of only using DC conductivity compared to AC conductivity

The AC conductivity of the FGT is strongly frequency dependent at low electric fields, as shown in Section 4.4. Those measurements are time consuming, and it is valuable to compare if it is sufficient to measure the DC conductivity and use as input to simulations. The conductivity is frequency independent at high electric fields, thus making the use of DC conductivity only valid at high electric fields. The simulated surface temperature and surface electric field by utilizing either AC or DC conductivity are shown in Figure 4-15 for the three FGTs at 50 Hz, 1 and 9 kHz. The main observation is that there is basically no difference in surface temperature between using AC or DC conductivity, neither at 50 Hz nor 1 kHz. The electric field distribution is also almost identical. This is due to minor difference between the AC and DC conductivity at those low frequencies. However, increasing further to 9 kHz, the surface temperature is overestimated by using the DC conductivity and the electric field is much less graded. The overall trend is comparable, but inaccurate values are expected to be obtained if the DC conductivity is used for calculations at high frequencies. This is a smaller problem for the surface temperature than the electric field.

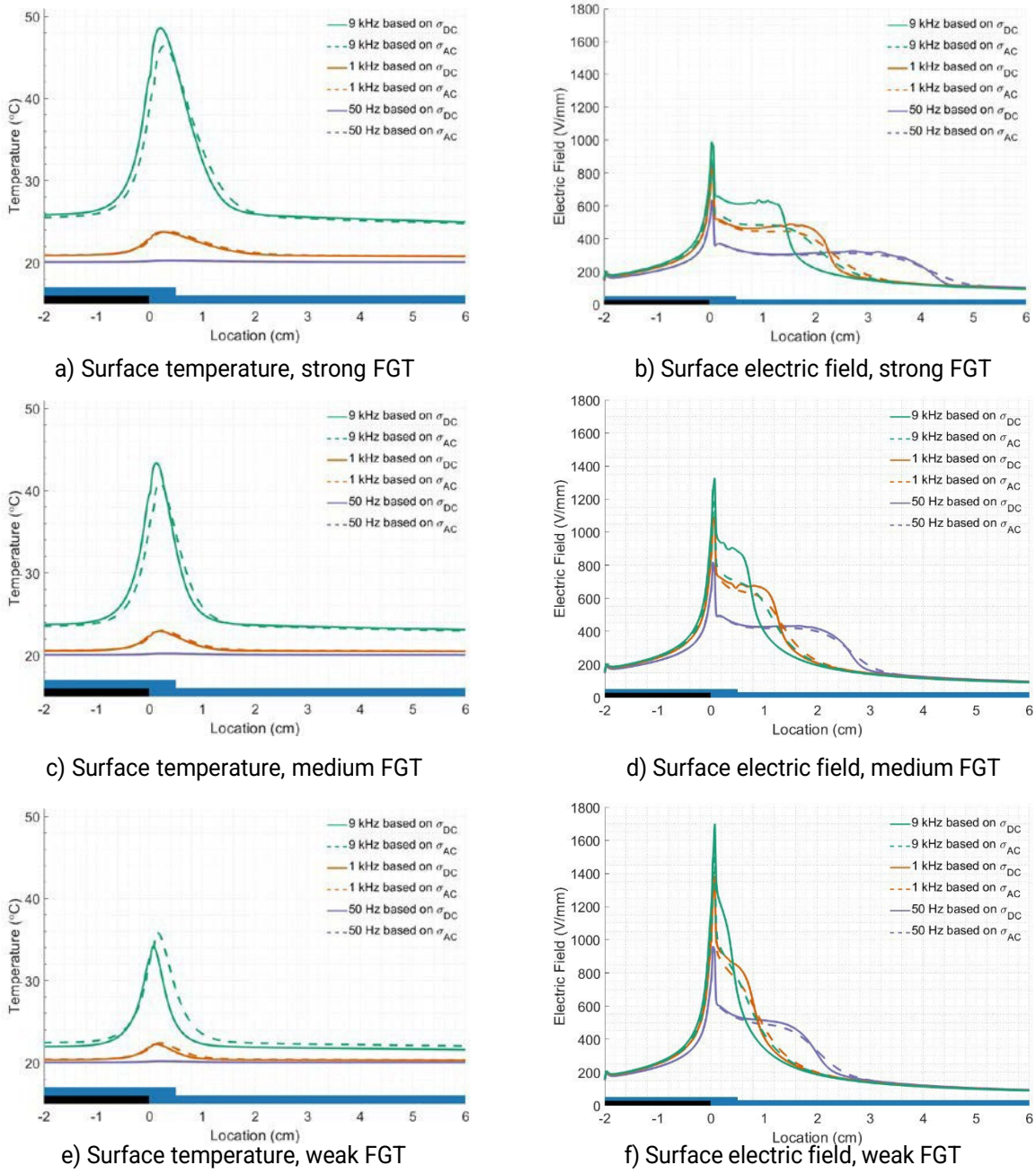

a) Surface temperature, strong FGT

b) Surface electric field, strong FGT

c) Surface temperature, medium FGT

d) Surface electric field, medium FGT

e) Surface temperature, weak FGT

f) Surface electric field, weak FGT

Figure 4-15: Simulated surface temperature and electric field as a function of spatial location at 50 Hz, 1 kHz, and 9 kHz for the strong, medium, and weak FGT. The curves are based on either AC or DC conductivity.

5 Discussions and recommendations for optimal design

It is known that increasing the electrical conductivity decreases the electric field, while at the same time increasing the heat production and temperature of the FGT (Naeini, Cherney, and Jayaram 2019). The capacitive currents in the end-windings are relatively small at 50 Hz, which means that the temperature increase is not a big problem at 50 Hz. Increasing the frequency increases the capacitive currents, which leads to higher joule losses and more concentrated electric field grading. Using voltages with higher frequencies might be problematic with respect to unwanted heating and reduced field grading. Higher voltage frequencies are used when controlling the generator by a power electronic converter with a PWM waveform. The nature of this voltage shape is to use a square wave with high switching frequency of several kHz, thus problematically high frequencies. Task 4.4 has therefore focused on electric properties of FGTs under application of sinusoidal voltage with frequencies limited at 10 kHz. The focus has been to describe the frequency dependence of the surface electric field and surface temperature. These descriptions are then used to discuss recommendations for design of end-winding electric field grading.

5.1 Material properties

The measured thermal conductivity of the three FGTs and the insulation was temperature independent. The average values increased slightly with temperature; however, the spread was larger than this increase, thus no temperature dependence of the thermal conductivity can be attested. The insulation had the lowest thermal conductivity, at approximately 0.5 W/(m·K). The thermal conductivity of the three FGTs increased with strength, that is, lowest thermal conductivity for the weak FGT and highest thermal conductivity for the strong FGT. The main difference between the tapes are the conductive particles, which can be assumed to contribute to the thermal conductivity by their concentration.

The presented model for AC electrical conductivity fitted the experimental data well with R^2 close to 1. It is therefore assumed that the used equations are valid as input to the FEM model. The calculated curve fitted models for the electrical conductivity as a function of electric field are shown in Figure 5-1 for the three FGT at indicated frequencies. It is observed that the low field DC case is equal for the three FGTs. The three FGTs have different field dependence of the DC conductivity. The model uses a complex permittivity to explain the behaviour at low electric fields, which results in a frequency dependent conductivity. This means that the DC conductivity cannot describe the conductivity at 9 kHz as the value differs several decades from that at low fields. The DC conductivity totally dominates at high electric fields; thus, no frequency dependence of the conductivity is expected.

The field dependence is clearly the greatest difference between the three FGTs, where the strong FGT has the strongest field dependence and the weak FGT has the weakest field dependence, as expected. The complex permittivity is almost similar for the three FGTs, which means that there is practically no difference between the FGTs at low electric fields.

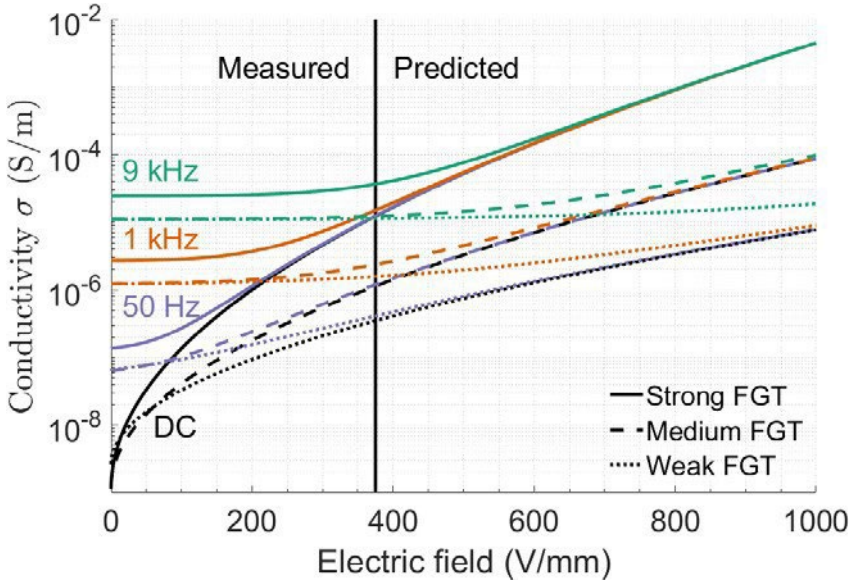

Figure 5-1: The model of the measured conductivity for the three FGTs at DC, 50 Hz, 1 kHz, and 9 kHz as a function of electric field.

5.2 Modelling

The modelling includes an electrical part with time scales of some tens of microseconds (10 kHz) and a thermal part with time scales in the range of minutes. It is time consuming to do simulations on a model including both the electrical and thermal parts. The thermal conductivity of the materials is temperature independent, whereas a parameter sweep shows that the heat capacity is insignificant. This enabled the modelling to be divided in two parts, one electrical with short time scale, and another thermal with long time scale.

The simulated results are dependent on geometry. The experimental test object was not a perfect cylinder: the FGT was wrapped around in a helix shape, and the conductivity was assumed isotropic. All these simplifications alter the accuracy of the model. Some difference between the simulated and measured values are therefore expected. Sharp edges are known to cause field enhancements, which means that if the COMSOL model has sharp edges where it should not have, it becomes unrealistic at elevated electric fields. That is, the maximum electric field is not reliable, whereas the electric field distribution is more reliable and is therefore used as a baseline for discussions. This means that the simulated results are not expected to be numerically totally accurate at high electric fields, however the trends provide valuable insight to the frequency dependence of the electric field and surface temperature.

Published literature uses mainly the DC conductivity of the FGT. This work has used the measured AC conductivity, as this is shown to be more accurate, see Section 4.8. It is possible to obtain the overall trends by using the DC conductivity, however small differences in the electric field calculations are expected. The simulations in this work employing the DC conductivity instead of the AC conductivity produce a slightly increased surface temperature at 9 kHz, whereas the electric field was less graded, meaning that the electric field is overestimated.

5.3 Comparison between measured and simulated surface temperature

The measured surface temperature is lower than the simulated surface temperature. The width of the temperature peak is greater for the measured surface temperature than the simulated surface temperature. The integrated temperature is, however, almost the same, where the measured temperature is slightly shifted towards the conductive OCP. That means that the total heat generation is the same distribution is different. The difference might originate in the insulating tape used to place the thermal sensors on the FGT. That could even the temperature distribution without altering the generated heat, which is dependent on the electric field conditions.

The overall small differences between the simulated and measured surface temperatures makes it therefore reasonable to rely on the simulated trends in the surface electric field.

5.4 Recommendations for design based on the current solution for 50 Hz

This work has described the frequency dependence of the conductivity, surface temperature, and surface electric field of the current design of end-windings that is optimized for 50 Hz. This has been done to make a foundation to answer the main goal of giving recommendations for design of end-winding electric field grading. A compilation of the main results for frequency dependent surface electric field peak width and surface temperature is given in Figure 5-2. The three FGTs have the exact same trends as a function of frequency. That is, increased temperature with increasing frequency and decreased electric field peak width with frequency. Overall, this results in a higher electric field and temperature with increasing frequency. The strong FGT has the highest field grading, however also the highest temperature, and the weak FGT has the lowest field grading and lowest temperature. This means that it is not possible to obtain good electrical and good thermal properties at the same time.

A FGT should be chosen based on the specific area of use. If cooling is not a problem, then a strong field grading can be beneficial, as the electric field is lower. If cooling is not effective, then a weaker field grading should be chosen because the heat production is lower. It can still be a difficult task, as the electric field might surpass the discharge threshold and surface discharges might occur. This can be more dangerous than the temperature rise as surface discharges might lead to breakdown on a much shorter time scale.

An interesting observation from Figure 5-2 is seen at 50 Hz where none of the FGTs experience temperature increase due to the electric field. The temperature increase is present at 1 kHz. For effective design, the choice of FGT is therefore dependent on the expected field levels at 50 Hz. The chosen design might be altered if higher frequencies are chosen, and surface temperature becomes more important than the surface electric field. In that case a weaker FGT is necessary. It is also worth noting that the peak width of the field grading of the strong FGT at 4 kHz is similar to the peak width of the weak FGT at 50 Hz. However, the surface temperature maximum is 34 °C compared to only 20 °C. Another similar relation can be seen for the peak width of the strong FGT at 9 kHz is the same as the peak width at 1 kHz for the medium FGT. However, the surface temperature difference is higher, 49 °C compared to just 23 °C.

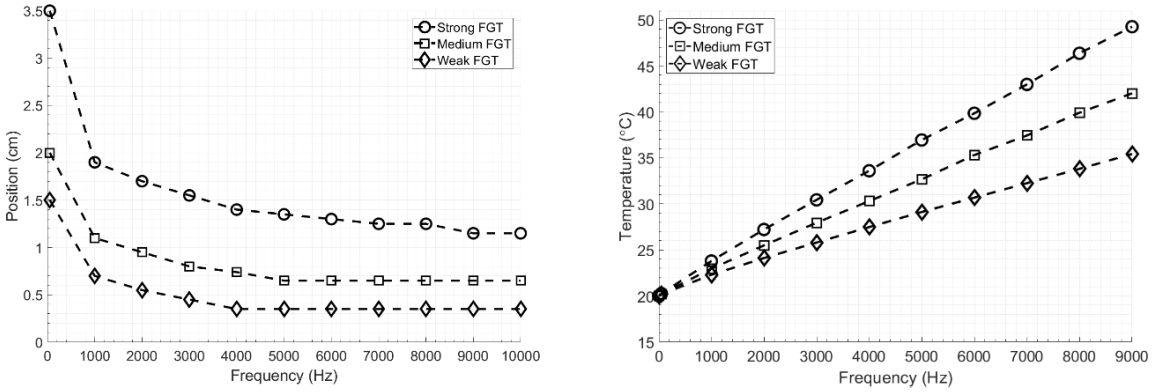

Figure 5-2: Compilation of previously presented electric field peak width (left) and surface temperature as a function of frequency. The strong FGT has the lowest average field in the high field region, however on the other hand the highest surface temperature. Weak FGT has the highest average field in the high field region, but the lowest surface temperature.

Increasing the service voltage frequency on the current 50 Hz solutions is going to reduce the field grading ability of the FGT. It can be to some extent be compensated by increasing the conductivity of the FGT, however at a cost of significantly higher surface temperature as more current flows though the insulation thus causing Joule heating. Proper cooling is therefore one solution to reduce the temperature. Another possibility is to reduce the switching frequency as much as possible to reduce temperature increase and not weaken the field grading.

6 Concluding remarks

Experimental work and numerical simulations of three field grading tapes (FGTs) have been used to create a foundation for discussing design of end-winding solutions for hydropower generator bars exposed to higher frequencies than 50 Hz. The main conclusions are summarized here:

- The thermal conductivities of both the FGTs and the insulation are temperature independent and increases with the electrical conductivity, indicating that the electrically conductive particles also are thermally conductive.
- The electrical conductivities of the FGTs are frequency and field dependent, which should be taken into account when modelling. It is, however, hardly temperature dependent in the range of 20 °C to 90 °C.
- The temperature independent parameters enable a less computationally demanding COMSOL model in two steps with different time constants, the electrical on microsecond scale, and the thermal on minute time scale.
- The simulated surface temperature is slightly different from the measured surface temperature. However, the integrated temperature is identical, indicating that the heat production in the experimental model and numerical model is the same.
- The use of AC conductivity in the numerical modelling is important at high frequencies, as the value is significantly higher than that of DC conductivity. Thus, using the DC conductivity results in overestimated surface temperature with higher electric field in a smaller region.
- The end-winding should be designed to be optimal to either the thermal or electrical properties. Both properties are not possible to optimize at the same time with the existing FGTs. The field grading is weakened, and the temperature is raised at frequencies as low as 1 kHz, which makes designing FGT for application of high frequencies a complicated task.

7 Publications from the project

1. Olav Henry Sagøy, "Dielectric Characterization of Semi-Conducting Field Grading Varnish for Hydro Generators" MSc Thesis, Norwegian University for Science and Technology (NTNU), 2020
2. Aakre et al. "Frequency and Temperature Dependence of Electric Field Grading on End-Winding of Generator Bars", 2022, Article in preparation.

8 Bibliography

Aakre, Torstein Grav. 2020. 'Partial Discharges in Voids at Variable Voltage Frequency and Temperature Diagnostic Testing of Stator Mainwall Insulation'. Trondheim, Norway: Norwegian Univeristy of Science and Technology (NTNU).

Amerpohl, Uwe, Matthias Kirchner, Bodo Böttcher, and Gerold Malin. 2002. 'Dry Type Outdoor Termination with New Stress Control Management'. In *Study Committee: 21 (Now B1)*. Paris, France.

Berlyand, L., and K. Golden. 1994. 'Exact Result for the Effective Conductivity of a Continuum Percolation Model'. *Phys. Rev. B* 50 (4): 2114—17. https://doi.org/10.1103/PhysRevB.50.2114.

Brandes, Heinz, Thomas Hillmer, and Peter Stebler. 2008. 'Halbleitende Lacke Und Bänder—Für Die Anwendung Nützliche Ergebnisse Und Eigenschaften'. *ETG-Fachbericht 110: Werkstoffe Mit Nichtlinearen Dielektrischen Eigenschaften*, 57–64.

Brütsch, R, and T Hillmer. 2006. 'Corona Protection in Rotating High Voltage Machines'. In . Berlin, Germany.

Cherney, E. A. 2005. 'Silicone Rubber Dielectrics Modified by Inorganic Fillers for Outdoor High Voltage Insulation Applications'. *IEEE Transactions on Dielectrics and Electrical Insulation* 12 (6): 1108–15. https://doi.org/10.1109/TDEI.2005.1561790.

Christen, Thomas, Lise Donzel, and Felix Greuter. 2010. 'Nonlinear Resistive Electric Field Grading Part 1: Theory and Simulation'. *IEEE Electrical Insulation Magazine* 26 (6): 47—59. https://doi.org/10.1109/MEI.2010.5599979.

Cigré, and Comité d'études D1. 2019. *FIELD GRADING IN ELECTRICAL INSULATION SYSTEMS*. Paris: Conseil international des grands réseaux électriques.

Cui, Lili, Xiaofeng Lu, Danming Chao, Hongtao Liu, Yongxin Li, and Ce Wang. 2011. 'Graphene-based Composite Materials with High Dielectric Permittivity via an in Situ Reduction Method'. *Physica Status Solidi (a)* 208 (2): 459—61.

Donzel, Lise, Felix Greuter, and Thomas Christen. 2011. 'Nonlinear Resistive Electric Field Grading Part 2: Materials and Applications'. *IEEE Electrical Insulation Magazine* 27 (2): 18–29. https://doi.org/10.1109/MEI.2011.5739419.

Donzel, Lise, M Montenegro-Uratsun, M Hagemeister, and P Rukwid. 2016. 'ZnO Stress Grading Tape for Stator Windings for Electrical Machines Located at Higher Altitudes'. In *Cigré Session 2016*, 12. Paris, France: Cigré. https://e-cigre.org/publication/D1-107_2016.

Espino-Cortes, F.P., E.A. Cherney, and S. Jayaram. 2005. 'Effectiveness of Stress Grading Coatings on Form Wound Stator Coil Groundwall Insulation Under Fast Rise Time Pulse Voltages'. *IEEE Transactions on Energy Conversion* 20 (4): 844—51. https://doi.org/10.1109/TEC.2005.853745.

Espino-Cortes, F.P., Cherney EA, and S.H. Jayaram. 2007. 'Impact of Inverter Drives Employing Fast-Switching Devices on Form-Wound AC Machine Stator Coil Stress Grading'. *IEEE Electrical Insulation Magazine* 23 (1): 16–28. https://doi.org/10.1109/MEI.2007.288451.

Espino-Cortes, F.P., S. Jayaram, and E.A. Cherney. 2006. 'Stress Grading Materials for Cable Terminations under Fast-Rise Time Pulses'. *IEEE Transactions on Dielectrics and Electrical Insulation* 13 (2): 430—35. https://doi.org/10.1109/TDEI.2006.1624289.

Glatz-Reichenbach, J., B. Meyer, R. Strümpler, P. Kluge-Weiss, and F. Greuter. 1996. 'New Low-Voltage Varistor Composites'. *Journal of Materials Science* 31 (22): 5941—44. https://doi.org/10.1007/BF01152143.

Gramespacher, Thomas Christen, Lise Donzel, and Felix Greuter. 2003. 'Microvaristor Based Field Grading Elements for HV Terminations'. In . Paris, France.

http://www.jicable.org/TOUT_JICABLE_FIRST_PAGE/2003/2003-A6-3_page1.pdf.

Greuter, F., and G. Blatter. 1990. 'Electrical Properties of Grain Boundaries in Polycrystalline Compound Semiconductors'. *Semiconductor Science and Technology* 5 (2): 111—37. https://doi.org/10.1088/0268-1242/5/2/001.

Greuter, F., M. Siegrist, P. Kluge-Weiss, R. Kessler, L. Donzel, R. Loitzl, and H. J. Gramespacher. 2004. 'Microvaristors: Functional Fillers for Novel Electroceramic Composites'. *Journal of Electroceramics* 13 (1): 739–44. https://doi.org/10.1007/s10832-004-5185-9.

Haverkamp, Wolfgang, Robert Strobl, and Gerold Malin. 2000. 'I\(0\)XSU-F - Neue Generation 6 Wärmeschrumpfender Mittelspannungsendverschlüsse Basierend Auf ZnO-Technologie,Elektrizitätswirtschaft <Frankfurt, Main>, Elektrizitätswirtschaft : EW ; Das Magazin Für Die Energiewirtschaft'. *Elektrizitätswirtschaft <Frankfurt, Main>, Elektrizitätswirtschaft : EW ; Das Magazin Für Die Energiewirtschaft*, Elektrizitätswirtschaft <Frankfurt, Main>, Elektrizitätswirtschaft : EW ; das Magazin für die Energiewirtschaft, 99 (26): 8—19.

Hayakawa, N., K. Kato, H. Hama, Y. Hoshina, and T. Rokunohe. 2014. 'Electric Field Grading Techniques in Power Apparatus Using Functional Materials'. In *CIGRE Paris Session*, D1-309.

Hu, Haitao, Xiaohong Zhang, Yanli Liu, Lijun Guo, and Junguo Gao. 2018. 'Optimization of the Electric Field Distribution at the End of the Stator in a Large Generator'. *Energies* 11 (10):2510. https://doi.org/10.3390/en11102510.

Huey, Bryan D., and Dawn A. Bonnell. 2000. 'Spatially Localized Dynamic Properties of Individual Interfaces in Semiconducting Oxides'. *Applied Physics Letters* 76 (8): 1012—14. https://doi.org/10.1063/1.125923.

Ishibe, Shinji, Masafumi Mori, Masahiro Kozako, and Masayuki Hikita. 2013. 'A New Concept Varistor with Epoxy/Microvaristor Composite'. *IEEE Transactions on Power Delivery* 29 (2): 677–82.

Jonsson, Erik, and Lars Palmqvist. 2008. A field grading material. European Patent Office EP 1 975 949 A1, filed 30 March 2007, and issued 1 October 2008. https://patentimages.storage.googleapis.com/5f/2d/06/bc20f954d821a5/EP1975949A1.pdf.

Kimura, K., and S. Hirabayashi. 1985. 'Improved Potential Grading Methods with Silicon Carbide Paints for High Voltage Coils'. *IEEE Transactions on Electrical Insulation* EI-20 (3): 511–17. https://doi.org/10.1109/TEI.1985.348775.

Lupo, G., V. Tucci, and M. Vitelli. 1995. 'Stress Control Tubes for HV Cable Terminations with Linear and Non Linear Characteristics: Theoretical and Experimental Approaches'. In *Subject 7; High Voltage Applications; Environmental Technologies; Cryogenic Insulation; New Technologies; INTERNATIONAL SYMPOSIUM ON HIGH VOLTAGE ENGINEERING;*
9th International Symposium; Subject 7; High Voltage Applications; Environmental Technologies; Cryogenic Insulation; New Technologies; 7869—71. Graz: Institute of High Voltage Engineering, Graz University of Technology; https://www.tib.eu/de/suchen/id/BLCP%3ACN011604857.

Mackevich, J. P., and J. W. Hoffman. 1991. 'Insulation Enhancement with Heat-Shrinkable Components. III. Shielded Power Cable'. *IEEE Electrical Insulation Magazine* 7 (4): 31–40. https://doi.org/10.1109/57.87659.

Mårtensson, Eva. 2003. 'Modelling Electrical Properties of Composite Materials'. Doctoral thesis, comprehensive summary, Stockholm: Elektrotekniska system. DiVA. http://urn.kb.se/resolve?urn=urn:nbn:se:kth:diva-3594.

Meyer, L. H., E. A. Cherney, and S. H. Jayaram. 2004. 'The Role of Inorganic Fillers in Silicone

Rubber for Outdoor Insulation Alumina Tri-Hydrate or Silica'. *IEEE Electrical Insulation Magazine* 20 (4): 13—21. https://doi.org/10.1109/MEI.2004.1318835.

Mikrajuddin, A., F. G. Shi, S. Chungpaiboonpatana, K. Okuyama, C. Davidson, and J. M. Adams. 1999. 'Onset of Electrical Conduction in Isotropic Conductive Adhesives: A General Theory'. *Materials Science in Semiconductor Processing* 2 (4): 309—19. https://doi.org/10.1016/S1369-8001(99)00035-9.

Momen, G., and Masoud Farzaneh. 2011. 'Survey of Micro/Nano Filler Use to Improve Silicone Rubber for Outdoor Insulators'. *Rev.Adv.Mater.Sci* 27: 1—13.

Naeini, Alireza, Edward. A. Cherney, and Shesha H. Jayaram. 2019. 'Effect of Conductivity on the Thermal and Electrical Properties of the Stress Grading System of an Inverter-Fed Rotating Machine'. *IEEE Transactions on Dielectrics and Electrical Insulation* 26 (1): 179–86. https://doi.org/10.1109/TDEI.2018.007618.

Nakamura, Shuhei, Kazuhiko Saito, Goro Sawa, and Keiichi Kitagawa. 1997. 'Percolation Threshold of Carbon Black-Polyethylene Composites'. *Japanese Journal of Applied Physics* 36 (Part 1, No. 8): 5163—68. https://doi.org/10.1143/jjap.36.5163.

Nan, C.-W., Y. Shen, and Jing Ma. 2010. 'Physical Properties of Composites Near Percolation'. *Annual Review of Materials Research* 40 (1): 131–51. https://doi.org/10.1146/annurev-matsci-070909-104529.

Nelson, P. N., and H. C. Hervig. 1984. 'High Dielectric Constant Materials For Primary Voltage Cable Terminations'. *IEEE Transactions on Power Apparatus and Systems* PAS-103 (11): 3211–16. https://doi.org/10.1109/TPAS.1984.318558.

Onneby, C., E. Martensson, U. Gafvert, A. Gustafsson, and L. Palmqvist. 2001. 'Electrical Properties of Field Grading Materials Influenced by the Silicon Carbide Grain Size'. In *ICSD'01. Proceedings of the 20001 IEEE 7th International Conference on Solid Dielectrics (Cat. No.01CH37117)*, 43–45. https://doi.org/10.1109/ICSD.2001.955507.

Pang, Huan, Tao Chen, Gangming Zhang, Baoqing Zeng, and Zhong-Ming Li. 2010. 'An Electrically Conducting Polymer/Graphene Composite with a Very Low Percolation Threshold'. *Materials Letters* 64 (20): 2226—29.

Penneck, R J, and P Taylor. 1976. Materials having non-linear resistance characteristics. GB1433129A, filed 1 September 1972, and issued 22 April 1976. https://patents.google.com/patent/US4252692A/en.

Pradhan, Manoj, Helena Greijer, Göran Eriksson, and Mikael Unge. 2016. 'Functional Behaviors of Electric Field Grading Composite Materials'. *IEEE Transactions on Dielectrics and Electrical Insulation* 23 (2): 768—78. https://doi.org/10.1109/TDEI.2015.005288.

Rieux, N, and M Marugan. 2002. 'Non-Linear Conductive Polymers for Power Electronics Passive Components Design'. In *Proceedings of the 9th INSUCON, International Electrical Insulation Conference*, 124—27. Berlin, Germany: INSUCON 2002 Secretariat.

Rivenc, J. P., and T. Lebey. 1999. 'An Overview of Electrical Properties for Stress Grading Optimization'. *IEEE Transactions on Dielectrics and Electrical Insulation* 6 (3): 309—18. https://doi.org/10.1109/94.775616.

Roberts, A. 1995. 'Stress Grading for High Voltage Motor and Generator Coils'. *IEEE Electrical Insulation Magazine* 11 (4): 26–31. https://doi.org/10.1109/57.400761.

Roman, H. E., A. Bunde, and W. Dieterich. 1986. 'Conductivity of Dispersed Ionic Conductors: A Percolation Model with Two Critical Points'. *Phys. Rev. B* 34 (5): 3439—45. https://doi.org/10.1103/PhysRevB.34.3439.

Sarraute, S., O. T. Sørensen, B. F. Sørensen, and E. R. Hansen. 1999. 'Microstructure Dependent Thermophysical Properties of Ni—Zn Ferrite—BaTiO3 Functionally Graded Ceramics'. *Journal of Materials Science* 34 (1): 99–104. https://doi.org/10.1023/A:1004417708696.

Secklehner, M., R. Hussain, and V. Hinrichsen. 2017. 'Tailoring of New Field Grading Materials for HVDC Systems'. In *2017 INSUCON - 13th International Electrical Insulation Conference (INSUCON)*, 1—6. https://doi.org/10.23919/INSUCON.2017.8097174.

Secklehner, Maximilian, Maria Kosse, and Volker Hinrichsen. 2017. *Characterization of Fillers for HVDC Field Grading Materials*. Winnipeg: CIGRE SC D1 Kolloquium.

Senn, Florian. 2010. 'Untersuchung elektrisch halbleitender Maerialien fur den Einsatz in Glimmschutzsystemen rotierender Hochspannungsmaschinen'. PhD, Graz, Austria: Technische Universitat Graz.

———. 2012. 'Charakterisierung Der Nichtlinearen Widerstandseigenschaften von Endenglimmschutzsystemen Rotierender Hochspannungsmaschinen'. *E & i Elektrotechnik Und Informationstechnik* 129 (5): 306–13.

Shakweh, Y. 2001. 'MV Inverter Stack Topologies'. *Power Engineering Journal* 15 (3): 139—49. https://doi.org/10.1049/pe:20010305.

Sharifi, E., S. Jayaram, and E.A. Cherney. 2008. 'Capacitive Grading of 13.8 KV Form-Wound Motor Coil Ends for Pulse Width Modulated Drive Operation'. In *Conference Record of the 2008 IEEE International Symposium on Electrical Insulation*, 632—35. Vancouver, BC: IEEE. https://doi.org/10.1109/ELINSL.2008.4570411.

Sharifi, Emad, Shesha Jayaram, and Edward Cherney. 2010a. 'Temperature and Electric Field Dependence of Stress Grading on Form-Wound Motor Coils'. *IEEE Transactions on Dielectrics and Electrical Insulation* 17 (1): 264—70. https://doi.org/10.1109/TDEI.2010.5412026.

———. 2010b. 'AC Modeling and Anisotropic Dielectric Properties of Stress Grading of Form-Wound Motor Coils'. *IEEE Transactions on Dielectrics and Electrical Insulation* 17 (3): 694–700. https://doi.org/10.1109/TDEI.2010.5492240.

Sheng, Ping, and R. V. Kohn. 1982. 'Geometric Effects in Continuous-Media Percolation'. *Phys. Rev. B* 26 (3): 1331—35. https://doi.org/10.1103/PhysRevB.26.1331.

Staubach, C. 2012. *Synthetisch Basiertes Entwurfsverfahren Zur Elektro-Thermischen Optimierung Der Resistiv-Kapazitiven Potentialsteuerung Großer, Rotierender Maschinen*. Kölner Wiss.-Verlag. https://books.google.no/books?id=iPErLWO7nm4C.

Stauffer, D., and A. Aharony. 1994. *Introduction To Percolation Theory*. Taylor & Francis. https://books.google.no/books?id=v66pIleij5QC.

Stone, G. C., M. Sasic, D. Dunn, and I. Culbert. 2011. 'Motor and Generator Windings'. *IEEE Industry Applications Magazine* 17 (6): 29–36. https://doi.org/10.1109/MIAS.2011.942303.

Stone, G. C., and H. G. Sedding. 1993. 'In-Service Evaluation of Motor and Generator Stator Windings Using Partial Discharge Tests'. In *Conference Record of the 1993 IEEE Industry Applications Conference Twenty-Eighth IAS Annual Meeting*, 240–47 vol.1. https://doi.org/10.1109/IAS.1993.298930.

Struempler, R., P. Kluge-Weiss, F. Greuter, and P. Vincenzini. 1995. 'Smart Varistor Composites, Topical Symposium VI; 8th World Ceramics Congress and Forum on New Materials, Intelligent Materials and Systems'. In *Intelligent Materials and Systems; ADVANCES IN SCIENCE AND TECHNOLOGY, Topical Symposium VI; 8th World Ceramics Congress and Forum on New Materials; Intelligent Materials and Systems*; 10:15—22. Florence, Italy: TECHNA Srl; https://www.tib.eu/de/suchen/id/BLCP%3ACN009885146.

Strümpler, R., and J. Glatz-Reichenbach. 1999. 'FEATURE ARTICLE Conducting Polymer Composites'. *Journal of Electroceramics* 3 (4): 329–46. https://doi.org/10.1023/A:1009909812823.

Stucki, F., and F. Greuter. 1990. 'Key Role of Oxygen at Zinc Oxide Varistor Grain Boundaries'. *Applied Physics Letters* 57 (5): 446–48. https://doi.org/10.1063/1.103661.

Virsberg, L., and A Kelen. 1963. An electrically conducting varnish for application on the surfaceof an electrical insulation. GB917036(A), filed 21 June 1960, and issued 30 January 1963. https://patents.google.com/patent/GB917036A/en?oq=GB917036.

Virsberg, L., and P. H. Ware. 1967. 'A New Termination for Underground Distribution'. *IEEE Transactions on Power Apparatus and Systems* PAS-86 (9): 1129–35. https://doi.org/10.1109/TPAS.1967.291798.

Wang, Zepu, J. Keith Nelson, Henrik Hillborg, Su Zhao, and Linda S. Schadler. 2012. 'Graphene Oxide Filled Nanocomposite with Novel Electrical and Dielectric Properties'. *Advanced Materials* 24 (23): 3134—37. https://doi.org/10.1002/adma.201200827.

Weidner, J. 2008. 'Design Und Überwachung von Grenzflächen Bei Ständerwicklungen Großer Turbogeneratoren'. In , 127. Würzburg, Germany: VDE VERLAG GMBH.

Weidner, Jürgen R, Christian Staubach, and Guido Schmidt. 2011. 'Elektrische Feldsteuerung Bei Ständerwicklungen von Turbogeneratoren – Anforderungen, Berechnungsverfahren, Konstruktion, Betriebsverhalten'. In *Feldsteuernde Isoliersysteme*. Darmstadt, Deutschland: VDE Verlag.

Wheeler, J. C. G. 2005. 'Effects of Converter Pulses on the Electrical Insulation in Low andMedium Voltage Motors'. *IEEE Electrical Insulation Magazine* 21 (2): 22—29. https://doi.org/10.1109/MEI.2005.1412216.

Wheeler, J. C. G., A. M. Gully, A. E. Baker, and F. A. Perrot. 2007a. 'Novel Stress Grading Systems for Converter-Fed Motors'. *IEEE Electrical Insulation Magazine* 23 (1): 29–35. https://doi.org/10.1109/MEI.2007.288457.

———. 2007b. 'Thermal Performance of Stress Grading Systems for Converter-Fed Motors'. *IEEE Electrical Insulation Magazine* 23 (2): 5–11. https://doi.org/10.1109/MEI.2007.357804.

Xanthos, M. 2005. *Functional Fillers for Plastics*. Wiley-VCH. https://books.google.no/books?id=4b9TAAAAMAAJ.

Y.A. Cengel. n.d. *Heat Transfer: A Practical Approach*. 2nd ed. McGraw-Hill, New York. Yang, Xiao, Jinliang He, and Jun Hu. 2015. 'Tailoring the Nonlinear Conducting Behavior of Silicone Composites by ZnO Microvaristor Fillers'. *Journal of Applied Polymer Science* 132 (40). https://doi.org/10.1002/app.42645.

Yang, Xiao, Xiaolei Zhao, Jun Hu, and Jinliang He. 2018. 'Grading Electric Field in High Voltage Insulation Using Composite Materials'. *IEEE Electrical Insulation Magazine* 34 (1): 15— 25. https://doi.org/10.1109/MEI.2018.8246118.

Zhang, Mao-Hua, Lovro Fulanović, Sonja Egert, Hui Ding, Pedro B. Groszewicz, Hans-Joachim Kleebe, Leopoldo Molina-Luna, and Jurij Koruza. 2020. 'Electric-Field-Induced Antiferroelectric to Ferroelectric Phase Transition in Polycrystalline NaNbO3'. *Acta Materialia* 200: 127—35. https://doi.org/10.1016/j.actamat.2020.09.002.

Zlupko, John E. 1976. Method of making an insulator with a non-linear resistivity coating of glass bonded silicon carbide. US Patent 3,982,048, filed 3 November 1975, and issued21 September 1976.

Appendix 1: Numerical testing

Parameter sweeps were performed to confirm that the relative permittivity and thermal conductivity of the OCP and the specific heat of the different materials did not affect the simulations significantly. A parameter sweep of the OCP relative permittivity value is shown in Figure A-1 and Figure A-2, whereas the heat capacity sweep is shown in Figure A-3, and the thermal conductivity sweep of the OCP is shown in Figure A-4 and Figure A-5. The conclusion is clear: These parameters have no significant influence on either the electric field or the surface temperature.

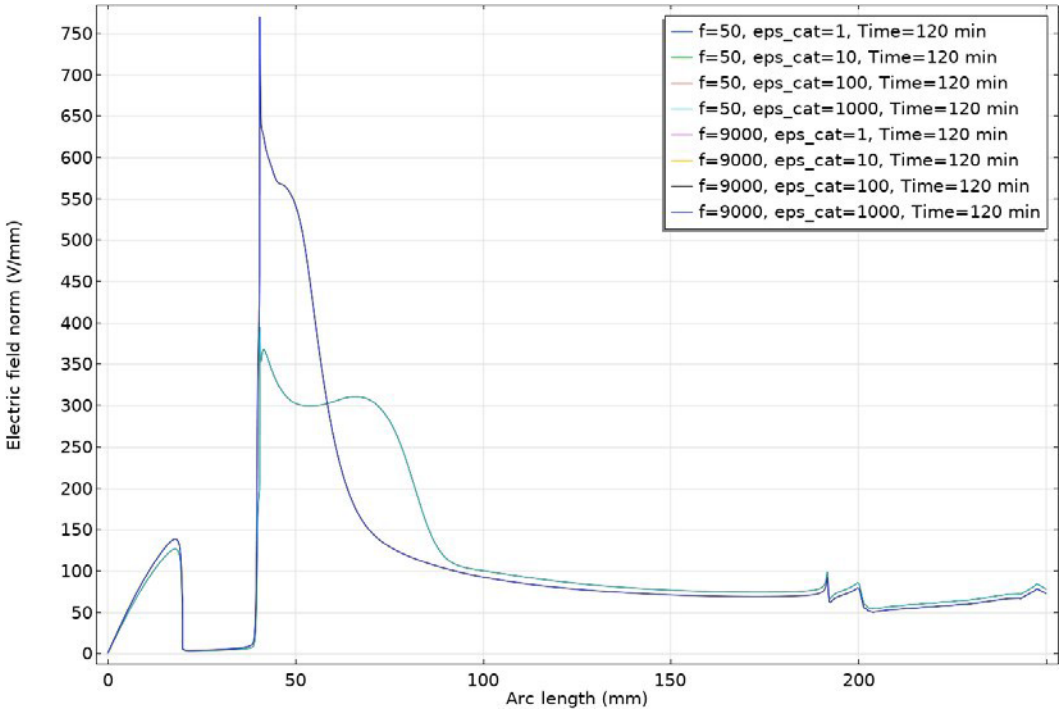

Figure A-1: Electric field as a function of spatial position for different relative permittivities for the OCP.The applied peak voltage is 5.5 kV with frequencies 50 and 9000 Hz.

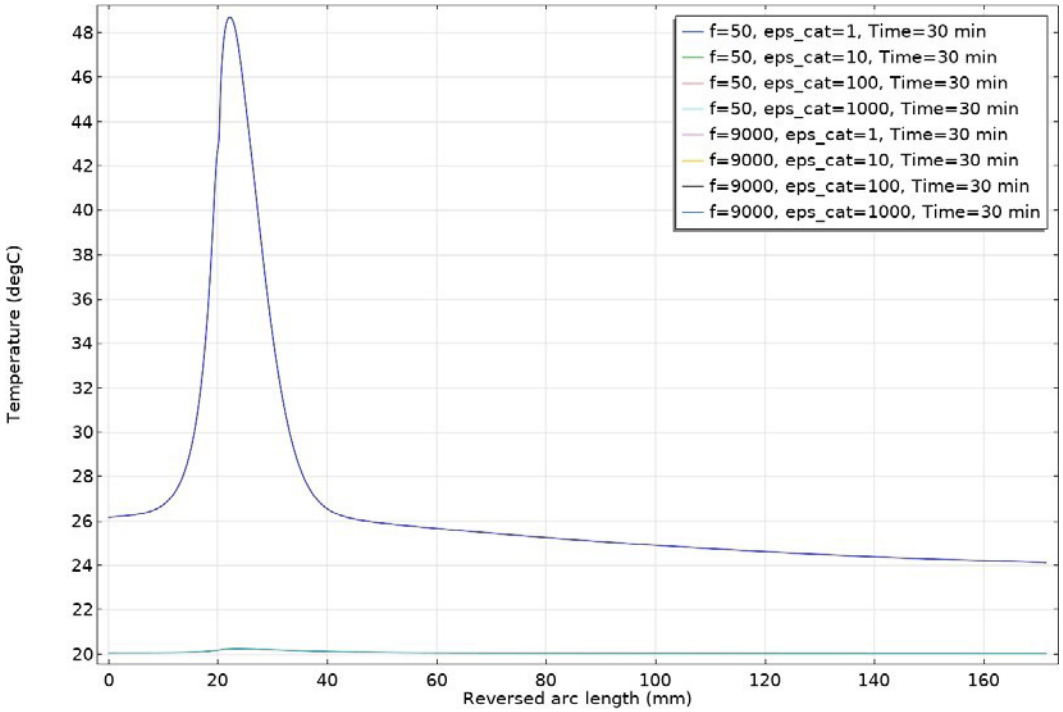

Figure A-2: Temperature as a function of spatial position for different relative permittivities for the OCP.The applied peak voltage is 5.5 kV with frequencies 50 and 9000 Hz.

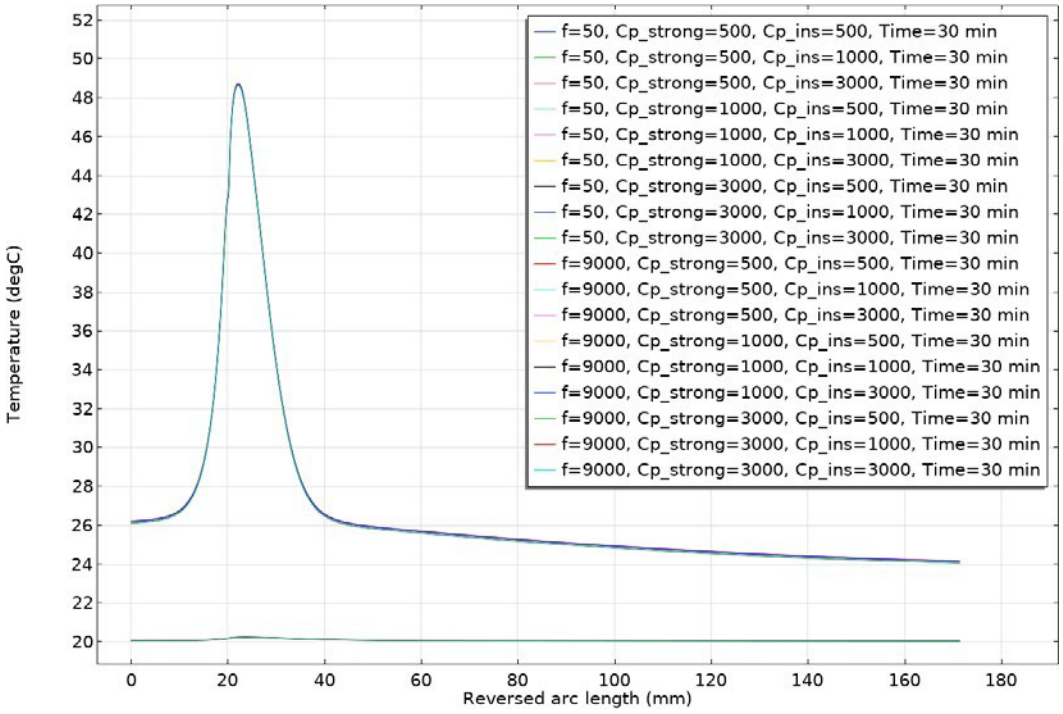

Figure A-3: Temperature as a function of spatial position for different combinations of specific heats forthe insulation and the FGT for an applied peak voltage of 5.5 kV at frequencies 50 and 9000 Hz.

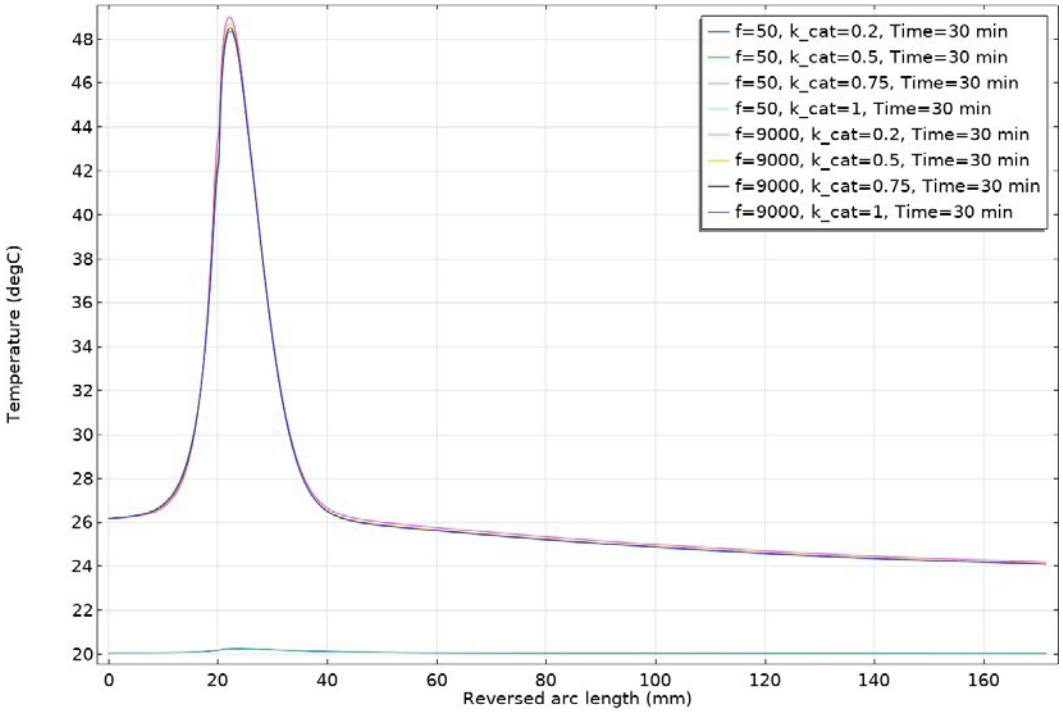

Figure A-4: Temperature as a function of spatial position for different thermal conductivity values for theOCP. The applied peak voltage is 5.5 kV with frequencies 50 and 9000 Hz.

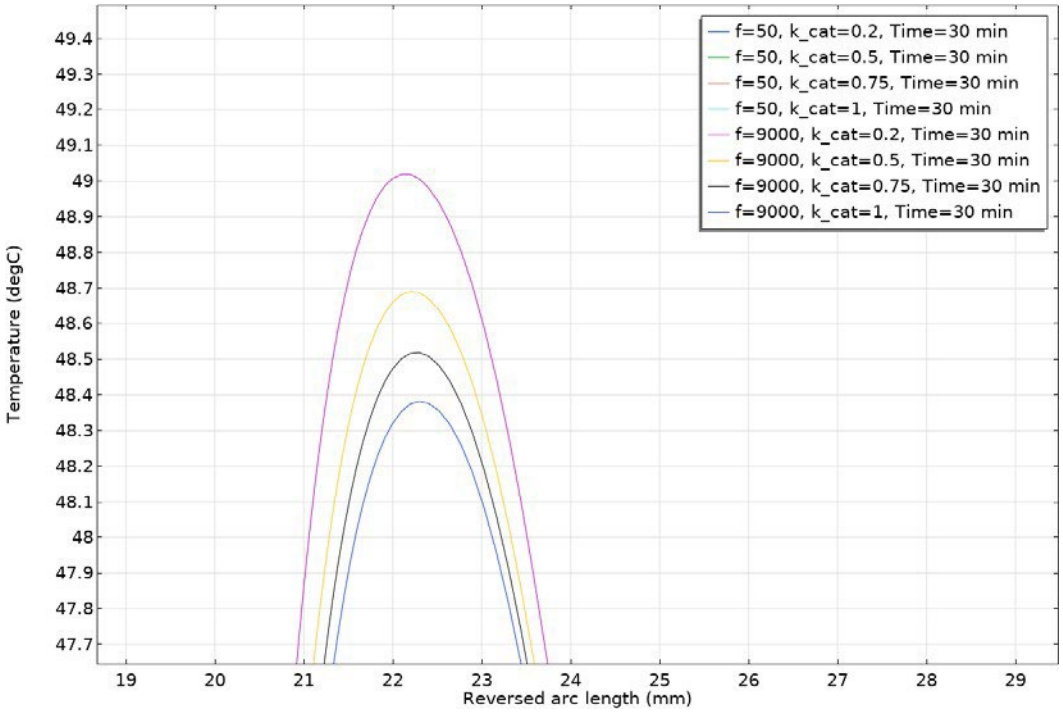

Figure A-5: Zoom in on the peak temperature as a function of spatial position for different thermal conductivity values for the OCP. The applied peak voltage is 5.5 kV with frequencies 50 and 9000 Hz. Thecurves from 50 Hz are below the lower y-value.